iScience

CellPress
OPEN ACCESS

Article

Multi-omic analysis reveals VEGFR2, PI3K, and JNK mediate the small molecule induction of human iPSC-derived cardiomyocyte proliferation

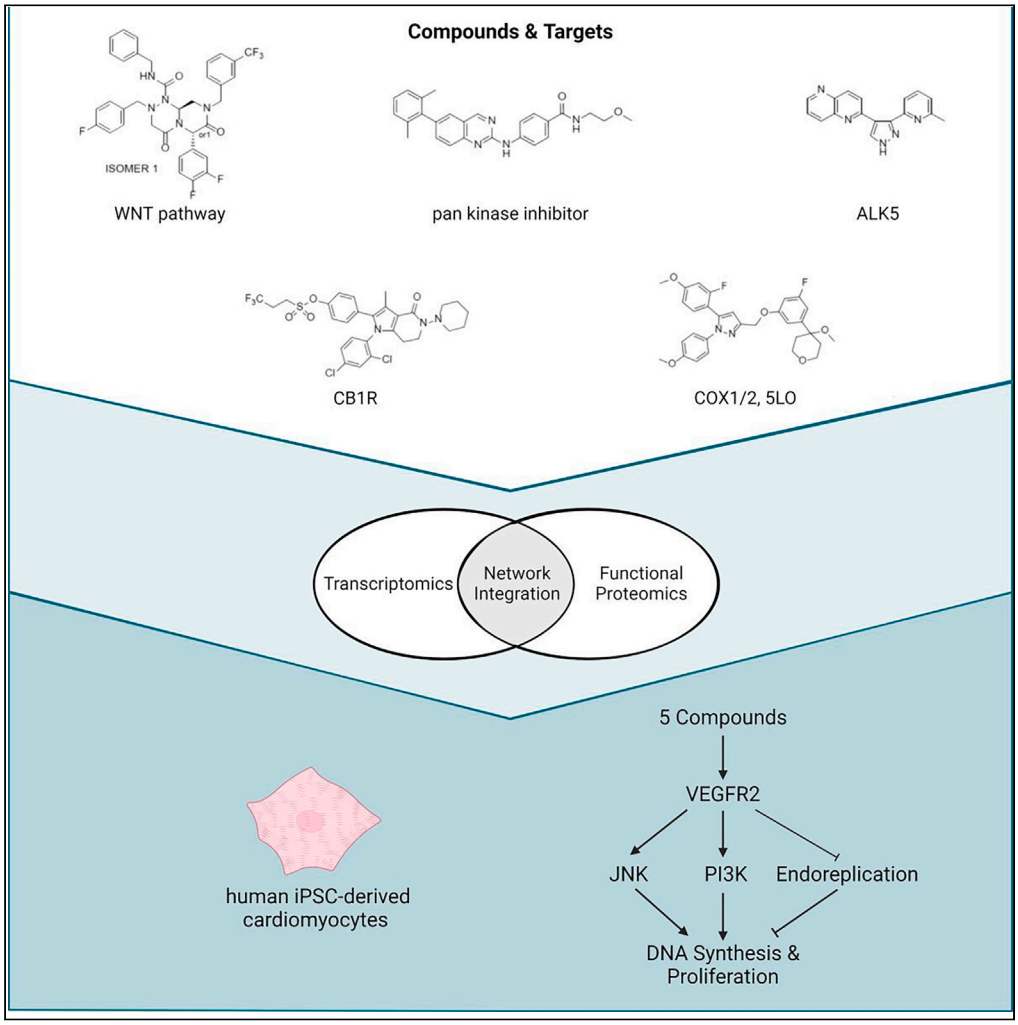

Laura A. Woo, Kaitlyn L. Wintruba, Bethany Wissmann, ..., Stefan Bekiranov, Qing-Dong Wang, Jeffrey J. Saucerman

jsaucerman@virginia.edu

Highlights

Five distinct compounds induce the proliferation of human iPSC-derived cardiomyocytes

Network analyses integrated transcriptomics and proteomics to identify common mechanisms

Experiments validated the roles of JNK and PI3K in compound-induced proliferation

The compounds induced VEGFR2 activity to limit endoreplication

Woo et al., iScience 27, 110485
August 16, 2024
https://doi.org/10.1016/j.isci.2024.110485

iScience

CellPress
OPEN ACCESS

Article

Multi-omic analysis reveals VEGFR2, PI3K, and JNK mediate the small molecule induction of human iPSC-derived cardiomyocyte proliferation

Laura A. Woo,[1] Kaitlyn L. Wintruba,[1] Bethany Wissmann,[1] Svyatoslav Tkachenko,[2] Ewa Kubicka,[3] Emily Farber,[8] Ola Engkvist,[4] Ian Barrett,[5] Kenneth L. Granberg,[6] Alleyn T. Plowright,[6] Matthew J. Wolf,[7] David L. Brautigan,[3] Stefan Bekiranov,[8] Qing-Dong Wang,[9] and Jeffrey J. Saucerman[1,10,*]

SUMMARY

Mammalian hearts lose their regenerative potential shortly after birth. Stimulating the proliferation of preexisting cardiomyocytes is a potential therapeutic strategy for cardiac damage. In a previous study, we identified 30 compounds that induced the bona-fide proliferation of human iPSC-derived cardiomyocytes (hiPSC-CM). Here, we selected five active compounds with diverse targets, including ALK5 and CB1R, and performed multi-omic analyses to identify common mechanisms mediating the cell cycle progression of hiPSC-CM. Transcriptome profiling revealed the top enriched pathways for all compounds including cell cycle, DNA repair, and kinesin pathways. Functional proteomic arrays found that the compounds collectively activated multiple receptor tyrosine kinases including ErbB2, IGF1R, and VEGFR2. Network analysis integrating common transcriptomic and proteomic signatures predicted that MAPK/PI3K pathways mediated compound responses. Furthermore, VEGFR2 negatively regulated endoreplication, enabling the completion of cell division. Thus, in this study, we applied high-content imaging and molecular profiling to establish mechanisms linking pro-proliferative agents to mechanisms of cardiomyocyte cell cycling.

INTRODUCTION

Technological advances in high-content imaging and automated image analysis have enabled rapid and efficient screening of therapeutic agents that enhance cardiomyocyte proliferation. Previous phenotypic screens of chemical compounds and microRNAs have identified numerous agents that stimulate cell cycle reentry and progression in murine[1,2] and human[3–5] cardiomyocytes, with many focusing on classical endpoint cell cycle markers (e.g., BrdU/EdU or Ki67). Postnatal mammalian cardiomyocytes can progress through unconventional cell cycles, such as endoreplication cycles, resulting in binucleated or polyploid phenotypes. Thus, assays using early cell cycle markers conflate cell cycle activity and authentic cardiomyocyte proliferation. Mature adult rodent[6,7] and human[8] hearts contain significant populations of binucleated or polyploid cardiomyocytes, respectively. Studies have reported binucleated and polyploid cardiomyocytes have lower proliferative capacities and limit cardiac regeneration *in vivo* compared to mononucleated diploid cardiomyocytes.[6,9,10] However, the biological significance of binucleation or polyploidization in the heart has yet to be determined. To address these limitations, we previously designed a high-content live-cell proliferation assay that discriminates between multiple cell cycle variants that generate new mononucleated diploid, binucleated, and polyploid hiPSC-CMs.[11]

While numerous targets, compounds, and microRNAs have been identified through phenotypic screens, the molecular mechanisms underlying the proliferative responses of such agents are often unknown.[1,2,5,11,12] A high-content phenotypic screen using a 3D human cardiac organoid system identified compounds that induced hiPSC-CM cell cycle reentry through mitosis without inducing binucleation or negatively

[1]Department of Biomedical Engineering and Robert M. Berne Cardiovascular Research Center, University of Virginia, Charlottesville, VA 22903, USA
[2]Quantitative Health Sciences, Lerner Research Institute, Cleveland Clinic Foundation, Cleveland, OH 44196, USA
[3]Center for Cell Signaling, Department of Microbiology, Immunology & Cancer Biology, University of Virginia, Charlottesville, VA 22903, USA
[4]Molecular AI, Discovery Sciences, R&D, AstraZeneca, 43150 Gothenburg, Mölndal, Sweden
[5]Data Sciences & Quantitative Biology, Discovery Sciences, R&D, AstraZeneca, Cambridge CB40WG, England
[6]Medicinal Chemistry, Research and Early Development, Cardiovascular, Renal and Metabolism, BioPharmaceuticals R&D, AstraZeneca, 43150 Gothenburg, Mölndal, Sweden
[7]Department of Medicine and Robert M. Berne Cardiovascular Research Center, University of Virginia, Charlottesville, VA 22903, USA
[8]Department of Biochemistry and Molecular Genetics, University of Virginia, Charlottesville, VA 22903, USA
[9]Bioscience Cardiovascular, Research and Early Development, Cardiovascular, Renal and Metabolism (CVRM), BioPharmaceuticals R&D, AstraZeneca, 43150 Gothenburg, Mölndal, Sweden
[10]Lead contact
*Correspondence: jsaucerman@virginia.edu
https://doi.org/10.1016/j.isci.2024.110485

Table 1. Lead compounds with annotated targets

Cpd ID	CAS #/AZ #	Public Domain	Alternative Name	Putative Targets	Structure
C1	1415655-56-9	Yes		WNT pathway	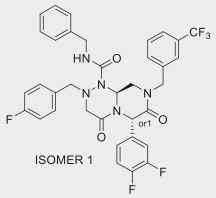
C2	AZ0001	No		pan kinase inhibitor	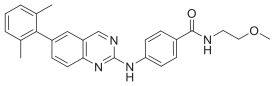
C3	446859-33-2	Yes	RepSox	ALK5	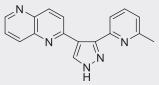
C4	932738-93-7	Yes	AZD2691	CB1R	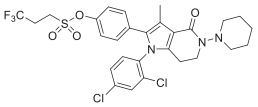
C5	AZ6538	No		COX1/COX2/5LO	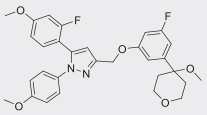

impacting contractile properties of the cardiac organoids.[5] Additional transcriptomic and proteomic analysis of four pro-proliferative compounds hitting distinct pathways revealed the mevalonate pathway as a core mediator of cardiomyocyte cell cycle progression.[5] Another group used high-content screens, RNA sequencing, and proteomic arrays to reveal cardiotoxic VEGFR2/PDGFR tyrosine kinase inhibitors triggered the compensatory activation of insulin/IGF1 signaling and the upregulation of VEGF receptor genes, that ultimately could be harnessed to promote hiPSC-CM survival.[13] These studies highlight unbiased molecular and phenotypic screening approaches that translate targets to mechanisms.

We previously performed a series of fixed and live-cell phenotypic screens that identified compounds inducing DNA synthesis and proliferation without enhancing binucleation or polyploidization in hiPSC-CMs.[11] In this study, we combine high-content phenotypic profiling and high-throughput multi-omic strategies to discover key mechanisms by which a diverse set of compounds stimulate proliferation in hiPSC-CMs. We selected five compounds, that were highly active in our phenotypic screens, with diverse putative targets including WNT, BRAF, ALK5, CB1R, and COX1/2. Putative targets represent the known compound targets that might mediate hiPSC-CM proliferation. Transcriptomic and proteomic analyses of these compounds identified a common set of differentially regulated transcription factors, proteins, and pathways including multiple RTKs. Network analysis integrating the common multi-omic signatures suggested multiple compound signals converged on canonical RTK pathway mediators JNK, MEK, and PI3K to promote hiPSC-CM proliferation. Additional perturbation experiments revealed key mechanisms regulating cardiomyocyte reentry, cell division, binucleation, and polyploidization.

RESULTS

Diverse lead compounds induce proliferation without multinucleation or polyploidy in hiPSC-cardiomyocytes

To investigate core mechanisms driving proliferation in human iPSC-derived cardiomyocytes (hiPSC-CMs), we selected five highly active compounds with diverse putative targets from a previous study that screened for DNA synthesis, proliferation, and endoreplication.[11] AstraZeneca's target annotation data indicated the lead compounds targeted WNT, BRAF, ALK5 (RepSox), CB1R (AZD2691), and COX-1/5-LO (Table 1). Using the same live-cell proliferation assay we developed in the previous study,[11] we confirmed the 5-point concentration-response profiles (0.1–10.0 μM) in three independent manufacturing lots of iCell Cardiomyocytes (Figure S1). Briefly, hiPSC-CMs were stained with a low, non-toxic concentration of Hoechst 33342, and the same imaging fields of view were collected at both initial (day 0) and final (day 6) timepoints. We quantified the change in the number of cells, binucleation events, and DNA content distribution using the image segmentation and analysis pipeline described in the previous study.[11] Consistent with the previous screens, all five compounds induced both DNA synthesis (Figures 1B and 1D) and proliferation (Figures 1C and 1E) without increasing the fraction of multinucleated

CellPress
OPEN ACCESS

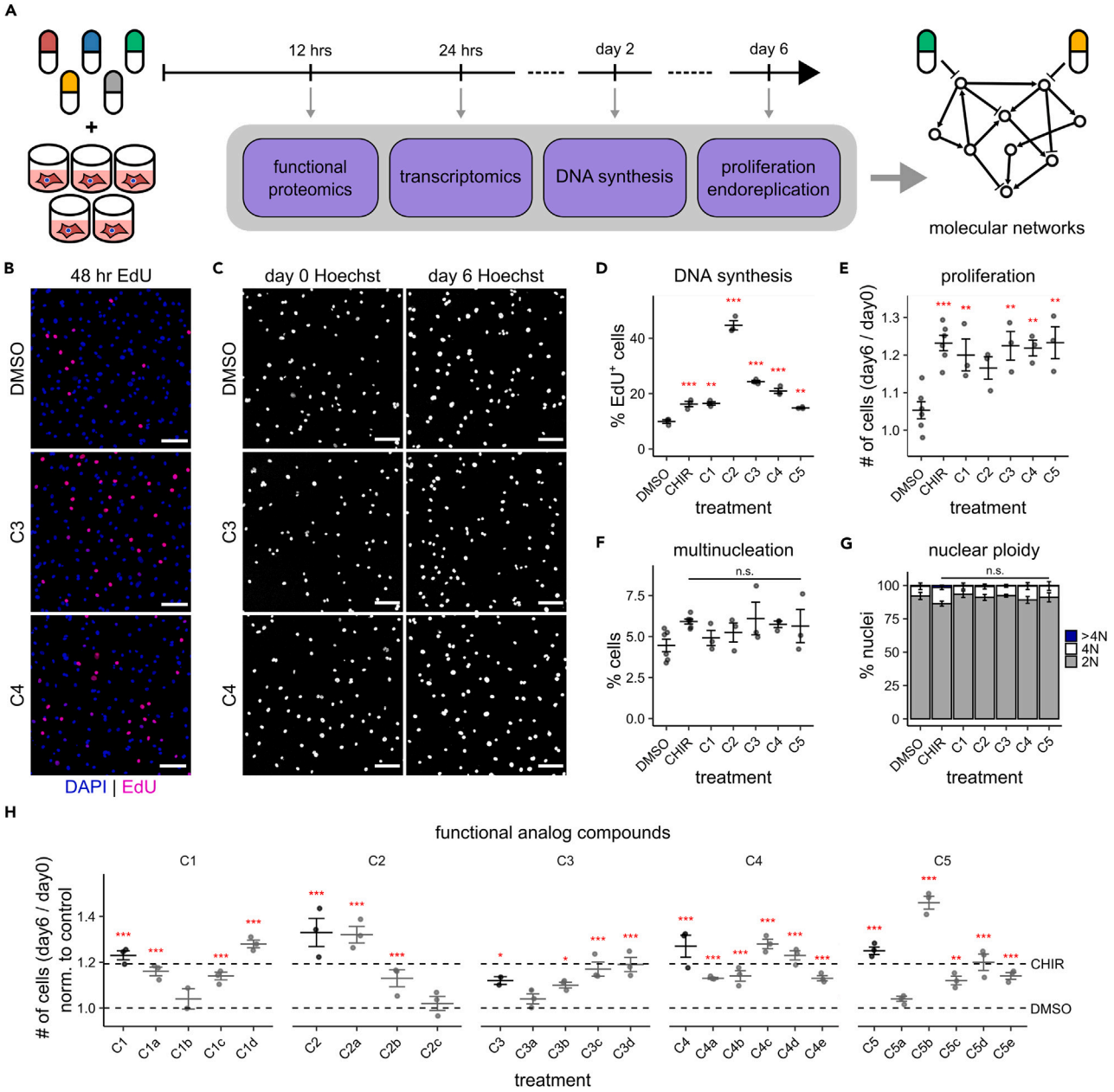

Figure 1. Five compounds targeting distinct pathways induce proliferation in hiPSC-CMs with minimal multinucleation and nuclear polyploidy

(A) Schematic of study.

(B) Representative images of 48 h EdU assay measuring DNA synthesis rates of hiPSC-CMs treated with a combination of compound and 1 μM EdU. Cells were fixed and stained with DAPI (blue) and EdU (magenta).

(C) Representative images of live-cell assay tracking changes in the number of cells over 6 days. Cells were stained with 0.02 μg/mL Hoechst and imaged on days 0 and 6.

(D and E) Quantification of B and C.

(F and G) Rate of multinucleation and (G) DNA content analysis, and (H) increase in number of cells after 6 days of treatment. Colors of stacked bar plots indicate ploidy states (2c, 4c, >4c) measured by the integrated intensity of Hoechst 33342. Treatments for (B-H) are as follows: negative control (0.1% DMSO), positive control (1 μM CHIR99021 aka CHIR), and maximum-effect concentrations for top five compounds (1 μM C1, 3.2 μM C2-C4, 10 μM C5). All experiments were performed using lot 3 of CDI iCell Cardiomyocytes. Scale bars are 100 μM. Error bars represent mean ± s.e.m. Stats for (D-G) were assessed by one-way ANOVA with Dunnett multiple comparisons test; n = 3–6; *$p < 0.05$, **$p < 0.01$, ***$p < 0.001$.

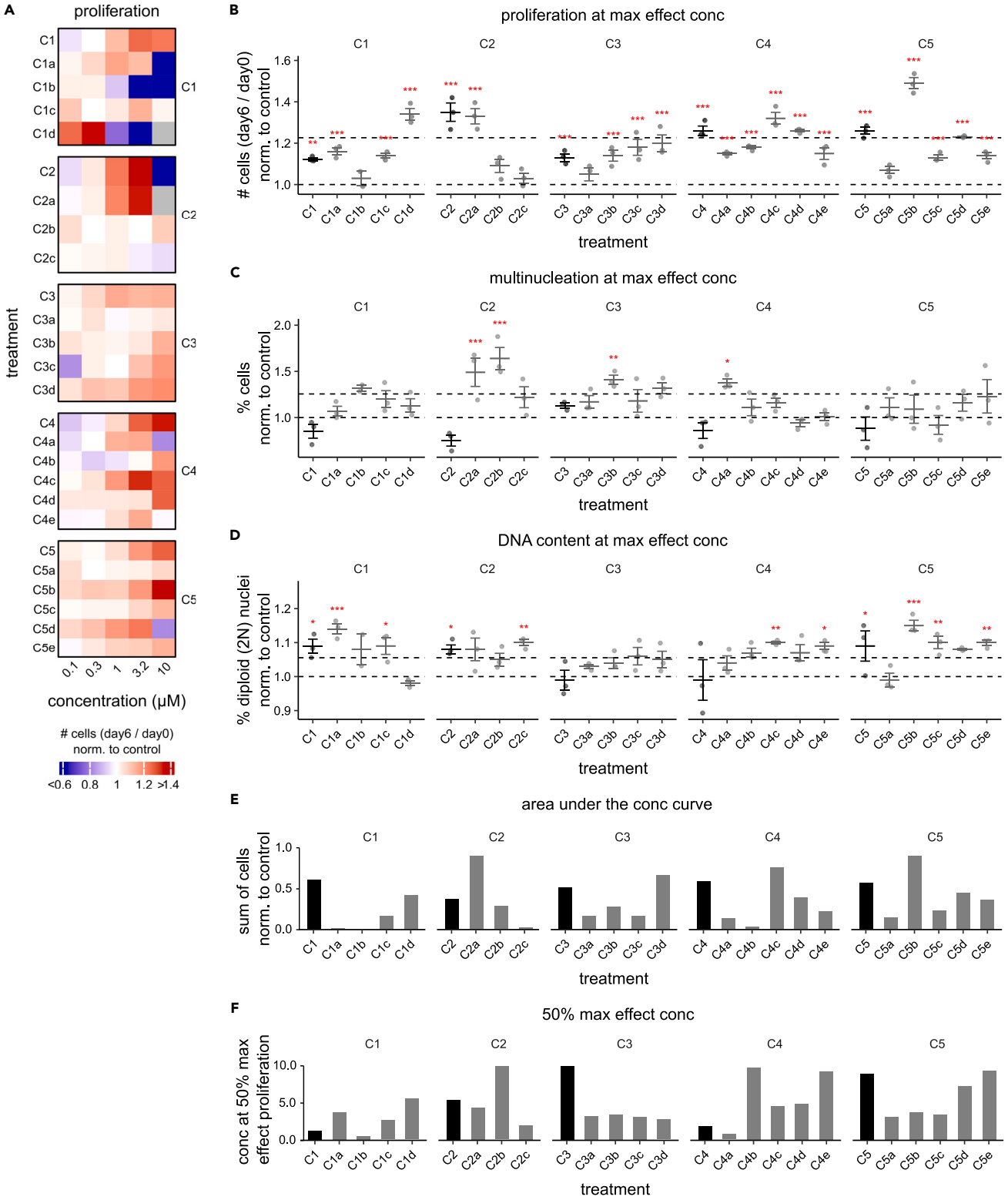

Figure 2. Functional analogs support putative targets of five lead compounds

(A) 5-point concentration responses (0.1–10 μM) of functional analogs to each of the top five compounds measuring the change in the number of cells over 6 days of treatment.

Figure 2. *Continued*

(B–F) Change in the number of cells, (C) rate of multinucleation, (D) fraction of diploid nuclei over 6 days of treatment at the maximum-effect concentrations for each compound, (E) area under the concentration response curve, and (F) concentration at 50% maximum-effect proliferation for each compound. (A–F) Metrics are normalized to the negative control (0.1% DMSO) on each plate. Functional analog compounds (gray) are identified by appending consecutive lower-case letters after lead compound (black) names. All plots are grouped by lead compound. Error bars represent mean ± s.e.m. Stats for (B–D) were assessed by one-way ANOVA with Dunnett multiple comparisons test; n = 2–24; $^{*}p < 0.05$, $^{**}p < 0.01$, $^{***}p < 0.001$.

cells (Figures 1F and S1) or polyploid nuclei (Figures 1G and 2C) at their respective maximal-effective (E_{max}) concentrations. Interestingly, while compound C2 induced the highest increase (over 4-fold) in the rate of DNA synthesis at 2 days compared to the negative control (Figure 1D), it produced the lowest gains in the number of new cells by day 6 (Figure 1C). This discordant response is also consistent with our previous study suggesting a moderate correlation between early DNA synthesis and late cell division metrics.[11] Among functional analogs for compound C1, C1 itself had the greatest overall efficacy and potency. In contrast, one or more functional analogs for compounds C2, C3, C4, and C5 exhibited event greater potency or efficacy than their corresponding lead compound (Figures 2E and 2F). Nonetheless, these five diverse compounds stimulated the proliferation of hiPSC-CMs.

To explore the potential for functional interactions between these lead compounds, we measured 6-day proliferation responses of all single and pairwise combinations of compounds C1-C4 at three concentrations each (0.1, 1.0, and 10.0 μM). We focused on assessing the responses of combination drugs at their single treatment E_{max} concentrations. Using the Highest Single Agent model,[14,15] we detected negative combination effects between C3 and C4 at 1.0 μM (Figure S2). No other significant effects were observed among the other combinations at E_{max}. This suggests compounds C3 and C4 act via common rather than largely separate intracellular downstream mechanisms.

To build our confidence in the putative targets, we tested three to five additional internal and commercially available functional analogs (Table S1) that have the same putative targets as each of the 5 lead compounds across five concentrations (Figure 2A). Using the live-cell proliferation assay, we confirmed more than two functional analogs for each of C1, C3, C4, and C5, which significantly increased proliferation over 6 days at E_{max} concentrations (Figure 2B), without increasing the rate of multinucleation (Figure 2C) or polyploidy (Figure 2D). Together, the above results demonstrate five lead compounds C1 through C5 that induce proliferation without additional endoreplication cycles in hiPSC-CMs. Additionally, based on their annotations and results with functional analogs, these results suggest that ALK5, CB1R, and COX-1/5-LO are regulators of hiPSC-CM proliferation.

Transcriptomic analysis exposes how lead compounds support a robust cell-cycle response

To elucidate molecular mechanisms driving the proliferative responses observed in the phenotypic assays, we performed bulk RNA sequencing on hiPSC-CMs treated with each of the five lead compounds. We sequenced the mRNA isolated from cells after 24 h of treatment at E_{max} concentrations. Over 11,000 differentially expressed genes (DEGs) were detected in at least one treatment compared to the DMSO negative control. Hierarchical clustering (Figure 3A) and principal component analysis (Figure 3B) of the transcriptome profiles demonstrated a high correlation within treatment groups, distinct from the negative control group. Differential expression analysis identified between ~3,500 and 7,000 DEGs for each compound, with 1,764 DEGs common to all five lead compounds (Figure 3C). We focused our attention on this group of common DEGs.

We next performed pathway enrichment analysis on the 1,764 common DEG set using Enrichr's bioinformatics tool and the Reactome database[16,17] to identify core pathways involved in regulating proliferation. In this common DEG set, 203 of 1,530 Reactome pathway modules were significantly enriched (adjusted $p \leq 0.05$). Consistent with the robust proliferation observed in the phenotypic experiments, Reactome's Cell Cycle module was the most significantly enriched (adjusted p 3.3×10^{-88}) by the common DEG set. In fact, the top 15 significantly enriched pathway modules by the common DEG set were related to cell cycle or DNA repair (Figure 3D). Cell cycle was also the most significantly enriched pathway using the KEGG 2019 Human library (adjusted p 2.6×10^{-24}), with 224 Cell Cycle genes expressed concordantly (Figure 3E). While the Reactome Cell Cycle genes accounted for only 12.7% of the common DEGs, excluding the Cell Cycle genes from the common DEG set reduced the total number of significantly enriched pathways down to three – DNA Repair, Fanconi Anemia Pathway, and Kinesins (Figure 3D).

To identify factors that may be driving these transcriptional responses, we next performed transcription factor (TF) enrichment analysis on the common DEG set using ChEA3's algorithm.[18] The top 15 predicted transcription factors included known cardiomyocyte cell-cycle regulators (e.g., E2F2,[19,20] FOXM1,[21–23] and MYBL2[24]) as well as transcriptional regulators not previously reported in the context of hiPSC-CM proliferation including E2F8 and CENPA (Figure 3F).

While DEGs common to all five lead compounds regulated cell cycle and DNA repair pathways, the compounds also elicited distinct transcriptional responses related to metabolism, FGF, and MAPK signaling (Figure S3B). Additionally, cell cycle pathways were noticeably absent from enrichment analysis performed with DEGs that are common to no more than 3 compounds. This suggests the commonalities among all five compounds are tightly linked to cell cycle regulation.

Functional proteomic profiling reveals the mechanistic role of receptor tyrosine kinases in regulating proliferation and endoreplication in response to compounds

We next analyzed the proteomic responses of hiPSC-CMs to the lead compounds to identify upstream proteomic signatures that may mechanistically link to downstream transcription. We used reverse phase protein arrays (RPPA) to measure the expression levels and phosphorylation status of 305 proteins in hiPSC-CMs treated for 12 h with each of the four lead compounds (C1, C3, C4, C5) at E_{max} concentrations. We

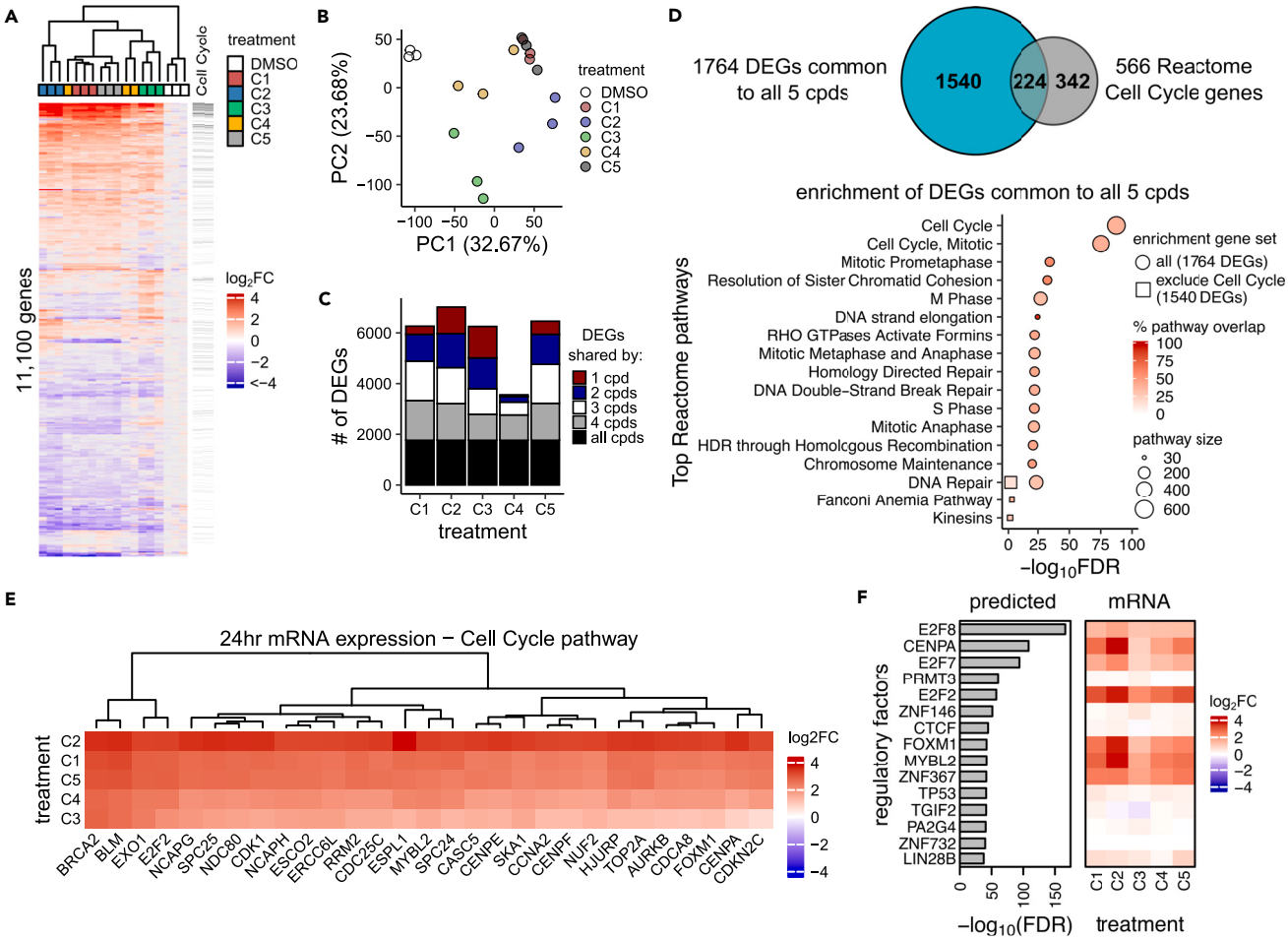

Figure 3. Transcriptomic analysis of proliferation-inducing compounds reveals a common and robust cell cycle response

(A) Hierarchical clustering of gene expression profiles and replicates of hiPSC-CMs treated with negative control (0.1% DMSO) and the top five compounds at maximum-effect concentrations (1 μM C1, 3.2 μM C2–C4, 10 μM C5). Only genes that are differentially expressed (FDR ≤0.05) compared to control in at least one compound are shown.

(B) Principal component analysis of data shown in (A).

(C) Distribution of DEGs that are unique (red) to each compound or common among 2–5 compounds.

(D) Enrichr's Reactome pathway enrichment analysis of the 1764 DEGs common to all five compounds (circles) and 1540 DEGs excluding the Reactome Cell Cycle gene set (squares). Top 15 pathways with FDR ≤0.1 are shown.

(E) Heatmap of $\log_2$ fold change of genes in Reactome's Cell Cycle pathway. Genes that are differentially expressed (FDR ≤0.05) in at least one compound are shown.

(F) ChEA3 transcription factor enrichment analysis of the 1764 common DEGs. Top 15 TFs rank-ordered by FDR with the corresponding mRNA expression profiles are shown. RNAseq was performed with $n = 3$ replicates.

found 109 significantly differentially expressed (FDR ≤0.05) probes in response to at least one compound (Figure 4A). Importantly, a common set of 17 probes exhibited concordant responses across all four compounds (Figure 4B). These probes include the upregulation of receptor tyrosine kinases (RTKs) including ErbB2 phosphorylation at Y1248 and total IGF1R expression. To further investigate the role of RTKs in compound-induced proliferation, we profiled the activity of 49 RTKs using a specialized array with the same protein lysates used for the RPPA. Consistent with the RPPA results, the RTK array confirmed the activation of ErbB2 and IGF1R in response to multiple compounds. VEGFR2 (KDR) was also consistently activated across all four compounds compared to the DMSO negative control (Figure 4C). Thus, despite having distinct molecular targets, these compounds induced the common activation of RTKs including ErbB2, IGF1R, and VEGFR2.

All three of these RTKs have been shown to be highly expressed in hiPSC-CMs,[13] and ErbB2[25–27] and IGF1R[28,29] have been previously implicated in promoting cardiomyocyte proliferation in other contexts. Furthermore, a phenotypic screen of growth factors revealed that VEGF ligands enhanced the proliferation of human iPSC-derived cardiac progenitor cells.[30] However, studies investigating the role of VEGF signaling in cardiomyocyte proliferation have been inconclusive and contradictory.[31–33] Thus, we decided to investigate the mechanistic role of RTK activation in mediating compound-induced proliferation. Tyrosine kinase inhibitors lapatinib, linsinitib, and axitinib were selected

CellPress
OPEN ACCESS

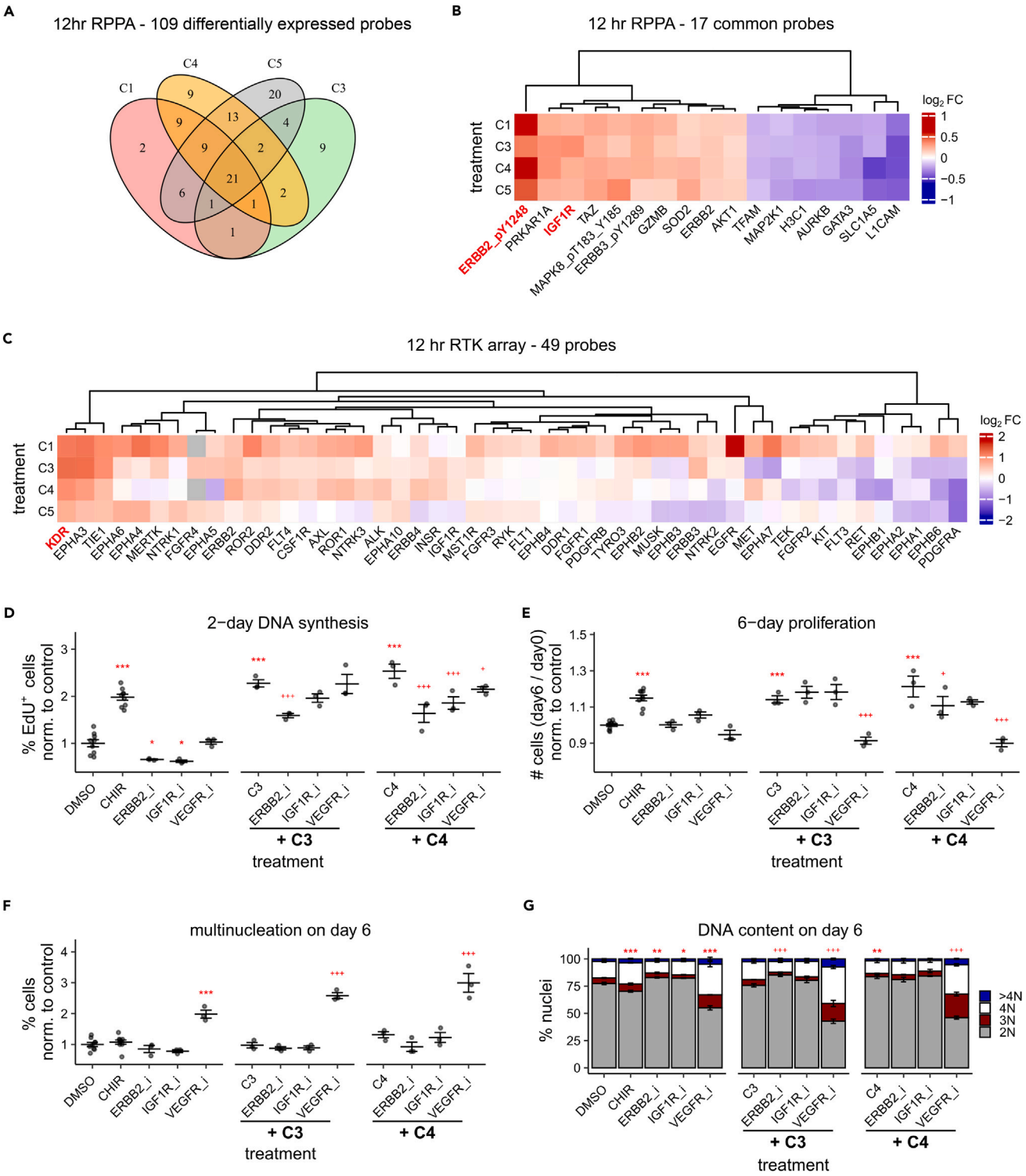

Figure 4. Functional proteomic profiling identifies a mechanistic role for receptor tyrosine kinases in response to pro-proliferative compounds

(A) Venn diagram of 109 significantly differentially expressed RPPA probes (FDR $\leq$0.05).

(B) Heatmap of unidirectional differentially expressed RPPA probes common to all 4 lead compounds. Log_2(fold change expression relative to DMSO control) is shown.

(C) Heatmap of 49 RTK probes measured using R&D's Human RTK array. Proteomic data shown in (A–C) were measured in hiPSC-CMs treated with the top 4 lead compounds (C1, C3, C4, and C5) for 12 h.

Figure 4. *Continued*

(D) 48 h EdU assay measuring DNA synthesis rates.

(E) 6-day live-cell proliferation assay tracking cell counts.

(F and G) Rate of multinucleation and G) DNA content after 6 days of treatment. Colors of stacked bar plots indicate DNA content levels (2c, 3c, 4c, >4c) measured by the integrated intensity of DAPI. Stats indicate significance for % 2c nuclei. Treatments for (D–G): negative control (0.1% DMSO), positive control (1 μM CHIR99021), and tyrosine kinase inhibitors targeting ERBB2 (1 μM lapatinib), IGF1R (0.1 μM linsitinib), VEGFR1/2/3 (10 μM axitinib) alone and in combination with 3.2 μM C3 or C4. Error bars represent mean ± s.e.m. Stats for (D-G) were assessed by one-way ANOVA with Benjamini-Hochberg FDR correction for select comparisons (* = all single treatments were compared to DMSO control; + = all combination treatments were compared to the respective lead compound C3 or C4); n = 3–9; *$p < 0.05$; **$p < 0.01$; ***$p < 0.001$.

to inhibit the activation of ErbB2/EGFR, IGF1R, and VEGF receptors, respectively. We used the 2-day EdU and 6-day live-cell proliferation assays to measure the effects on cell cycle progression in hiPSC-CMs. We found that inhibiting ErbB2 with 1 μM lapatinib attenuated both C3 and C4 induced DNA synthesis at 48 h (Figure 4D), but had little to no effect on proliferation by day 6 (Figure 4E). Similarly, inhibiting IGF1R with 0.1 μM linsitinib had a modest effect in reducing DNA synthesis (Figure 4D) in combination with C4 and no effect on late-stage proliferation metrics (Figure 4E). Conversely, the VEGF receptor inhibitor (10 μM axitinib) alone or in combination with C3 or C4 had little to no effect on early DNA synthesis (Figure 4D), but abrogated both C3 or C4 induced increase in cell numbers (Figure 4E). Surprisingly, the inhibition of the VEGF receptor resulted in over 2-fold increases in multinucleation (Figure 4F) and substantial decreases in the population of 2c nuclei (Figure 4G) compared to either the negative control or compound treatments alone. While VEGF receptor inhibition reduced cell numbers at times associated with cell cycle entry, by day 6, VEGFR inhibition in C3 or C4-treated hiPSC-CMs decreased nuclei number and circularity (Figure S4). Thus, the KDR expression induced by C3 and C4 may aid later proliferation but also induce cell survival pathways that limit stress-induced multinucleation and polyploidy.

Bivariate analysis of DNA content and Ki67 revealed this decrease in the diploid nuclei population was due to the decrease in the fraction of G0 diploid nuclei and corresponding increases in G0 intermediate DNA content and tetraploid populations (Figures 5B and 5C, and confirmed visually in Figure S5). Inhibition of these RTKs had no effect on overall cell cycle activity by day 6 (Figure 5A). Collectively, these results indicate the upregulation of the VEGF receptor plays an important role in preventing defects in cytokinesis, karyokinesis, and chromosome segregation in proliferating hiPSC-CMs. These results also suggest that both C3 and C4 mediate DNA synthesis and bona-fide proliferation via the activation of ErbB2 and VEGF receptors, respectively.

Network integration of multi-omic data identifies pathways that converge on JNK and PI3K

We next aimed to integrate the common proteomic signatures to downstream transcriptional regulators that drive cardiomyocyte proliferation. We sought to find causal relationships linking the set of the top 15 transcriptional regulators predicted from the RNAseq, 17 differentially expressed/activated proteins from the RPPA, and additional factors regulating proliferation confirmed by additional experimentation with the lead compounds. To reconstruct a directed signaling network, we used the SIGNOR database of manually annotated causal relationships[34,35] and the k shortest path algorithm from PATHLINKER,[36] with RTKs as source nodes and transcription factors as target nodes (Figure 6A). The overall direction of the proteomic responses measured by the RPPA and RTK arrays across all four compounds was mapped onto network nodes. The integrated molecular network suggested compounds activate ErbB2 and IGF1R pathways leading to the phosphorylation of RB1 and activation of E2F via the PI3K/AKT pathway. This would be expected to initiate cell cycle progression into S-phase, while inhibiting proteins associated with arresting or inhibiting the cell cycle such as CDKN1B. The network also predicts canonical RTK pathways, plus JNK, MEK, and PI3K, play an important role in mediating compound-induced proliferation.

We decided to further investigate MAPK and PI3K signaling pathways, which are known as key intermediates in RTK signal transduction and supported by our integrated network. We tested small molecule inhibitors targeting JNK, MEK, and PI3K in unstimulated and stimulated hiPSC-CMs. We used the same set of high-content assays to measure DNA synthesis at two days and cell division, multinucleation, DNA content, cell cycle phase distributions, and nuclear ploidy at six days post treatment with inhibitors. We found that inhibiting JNK with 10 μM SP600125, MEK with 10 μM PD98059, and PI3K with 10 μM LY294002 attenuated C3 and C4 induction of DNA synthesis at 48 h (Figure 6B). Inhibition of MEK and PI3K in unstimulated hiPSC-CMs resulted in modest decreases in EdU incorporation (Figure 6B). By day 6, only JNK and PI3K inhibition attenuated C3 and C4 induced proliferation, with none of the three kinase inhibitors affecting proliferation in unstimulated hiPSC-CMs (Figure 6C). Consistent with results from the RTK experiments, the overall increase in cell cycle activity was not sustained for 6 days (Figure 6D). The anti-proliferative effects observed with JNK and PI3K inhibition in stimulated hiPSC-CMs did not correlate with increased multinucleation, G0 intermediate DNA content, or G0 tetraploidy (Figure S6), suggesting that the VEGF receptor regulation of cardiomyocyte endoreplication is not mediated via these kinases. While DNA content analysis found a decrease in diploid (2c) nuclei for hiPSC-CMs treated with C4 and JNK inhibitor SP600125, bivariate analysis revealed this was mostly attributed to an increase in the population of G2/M 4c nuclei (Figure S6). Together, these results suggest that C3 and C4 compounds, which are known to target ALK5 and CB1 pathways respectively, converge on JNK, MEK, and PI3K pathways to regulate DNA synthesis and JNK and PI3K to complete cell division.

DISCUSSION

Pharmacological manipulation of signaling pathways to stimulate the proliferation of endogenous cardiomyocytes is a promising therapeutic strategy for cardiac regeneration. Further, cardiomyocyte binucleation and polyploidization have been linked to a loss of proliferative and

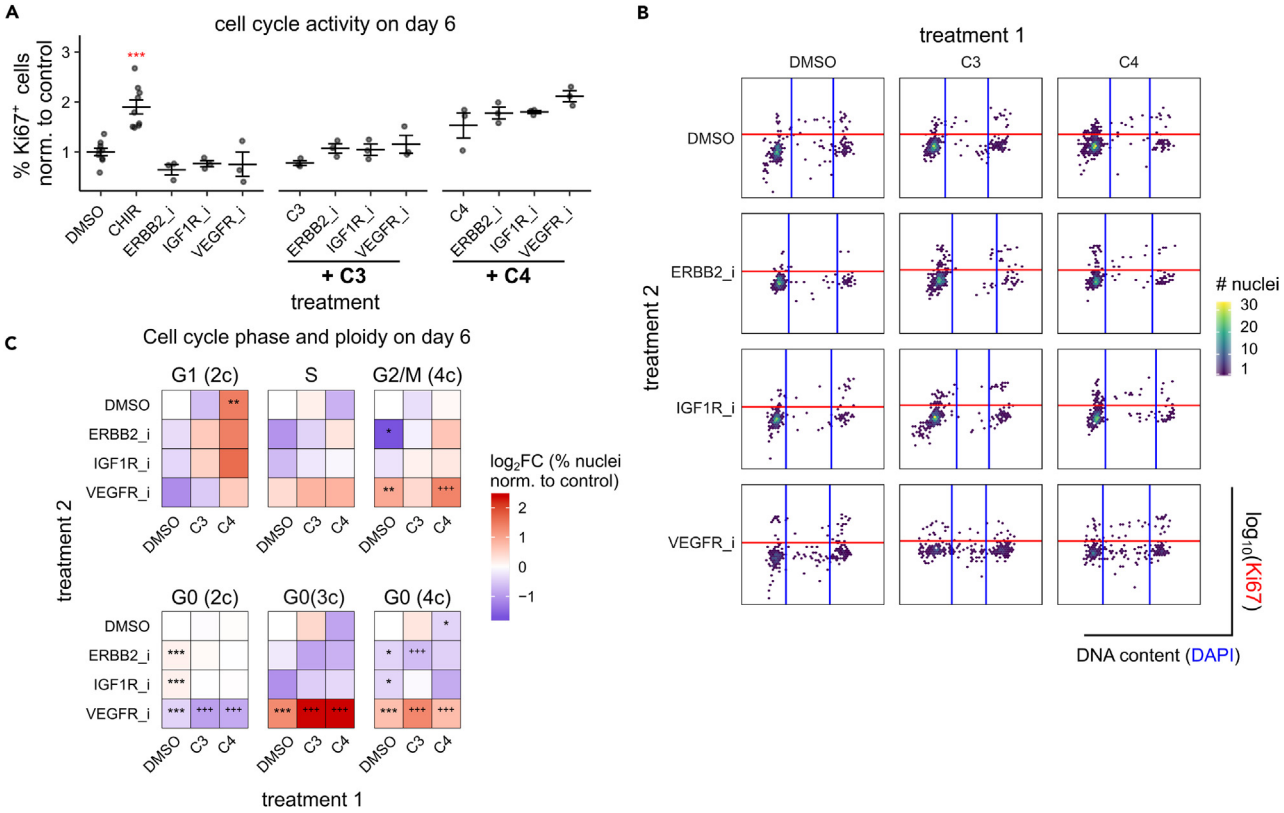

Figure 5. Compound-induced expression of VEGF receptors limits increases in ploidy

(A) Ki67 staining measuring cell cycle activity after 6 days of treatment.

(B) Bivariate analysis of DNA content (x axis) and Ki67 staining (y axis) to separate out cell cycle phase and nuclear ploidy levels. DNA content thresholds separating 2c, 3c, and 4c nuclei are shown as blue horizontal lines. Ki67 positive threshold is shown as a red horizontal line. Nuclei with <2c or >4c DNA content are not shown. Replicate with median G0 measurement is shown.

(C) Quantification of B. Treatments for (A–C): negative control (0.1% DMSO), positive control (1 μM CHIR99021), and small molecule inhibitors targeting ERBB2 (1 μM lapatinib), IGF1R (0.1 μM linsitinib), and VEGFR1/2/3 (10 μM axitinib) alone and in combination with 3.2 μM C3 or C4. Error bars represent mean ± s.e.m. Stats for (A and C) was assessed by one-way ANOVA with Benjamini-Hochberg FDR correction for select comparisons (* = all single treatments were compared to DMSO control; + = all combination treatments were compared to the respective lead compound C3 or C4); n = 3–9; *$p < 0.05$; **$p < 0.01$; ***$p < 0.001$.

regenerative potential.[9,10,27,37] In this study, we used a systems biology approach combining phenotypic, transcriptomic, and proteomic data to identify core mechanisms regulating hiPSC-CMs proliferation. Based on hits from a previous high-content screen of a small molecule library,[11] we selected five lead compounds with diverse putative targets for molecular profiling. We aimed to test whether multiple signals converge on common mechanisms to regulate cell cycle progression. Using high-throughput RNA sequencing and functional proteomic arrays, we identified a common set of transcriptional and proteomic responses mediating compound-induced proliferation and endoreplication. Integration of this multi-omic signature revealed a directed molecular network of canonical RTK pathways that were activated by multiple pro-proliferative compounds.

Characterizing mechanisms for cell cycle progression in cardiomyocytes beyond classical DNA synthesis and cell cycle markers is critical for identifying therapeutic agents that stimulate the proliferation of mononucleated diploid cardiomyocytes. In this study, we applied a high-content live-cell proliferation assay[11] to comprehensively assess the effects of pharmacological perturbations on proliferation, multinucleation, polyploidization, and cell cycle activity in hiPSC-CMs. We confirmed that five hits from our previous study stimulated proliferation while maintaining or enhancing the populations of mononucleated cells and diploid nuclei. Testing multiple functional analogs to each of the lead compounds substantiated putative inhibitory targets for compounds C3, C4, and C5, implicating type 1 transforming growth factor β receptor (ALK5), cannabinoid receptor type 1 (CB1R), and cyclooxygenase-1 and 2 (COX-1/2)/5-lipoxygenase (5-LO) as negative regulators of hiPSC-CM proliferation, respectively. We focused additional mechanistic experiments in stimulated hiPSC-CMs using inhibitors targeting receptors ALK5 (C3) and CB1R (C4). Complementary genetic perturbation studies can further validate the targets responsible for the observed effects of these compounds.

In support of the pro-proliferative responses to these lead compounds, enrichment analysis of the transcriptome profiles identified robust changes in the expression of genes involved in cell cycle regulation. Removal of these genes from the analysis revealed an underlying common transcriptional program regulating DNA repair and kinesin pathways. DNA damage that remains unrepaired can lead to cell-cycle

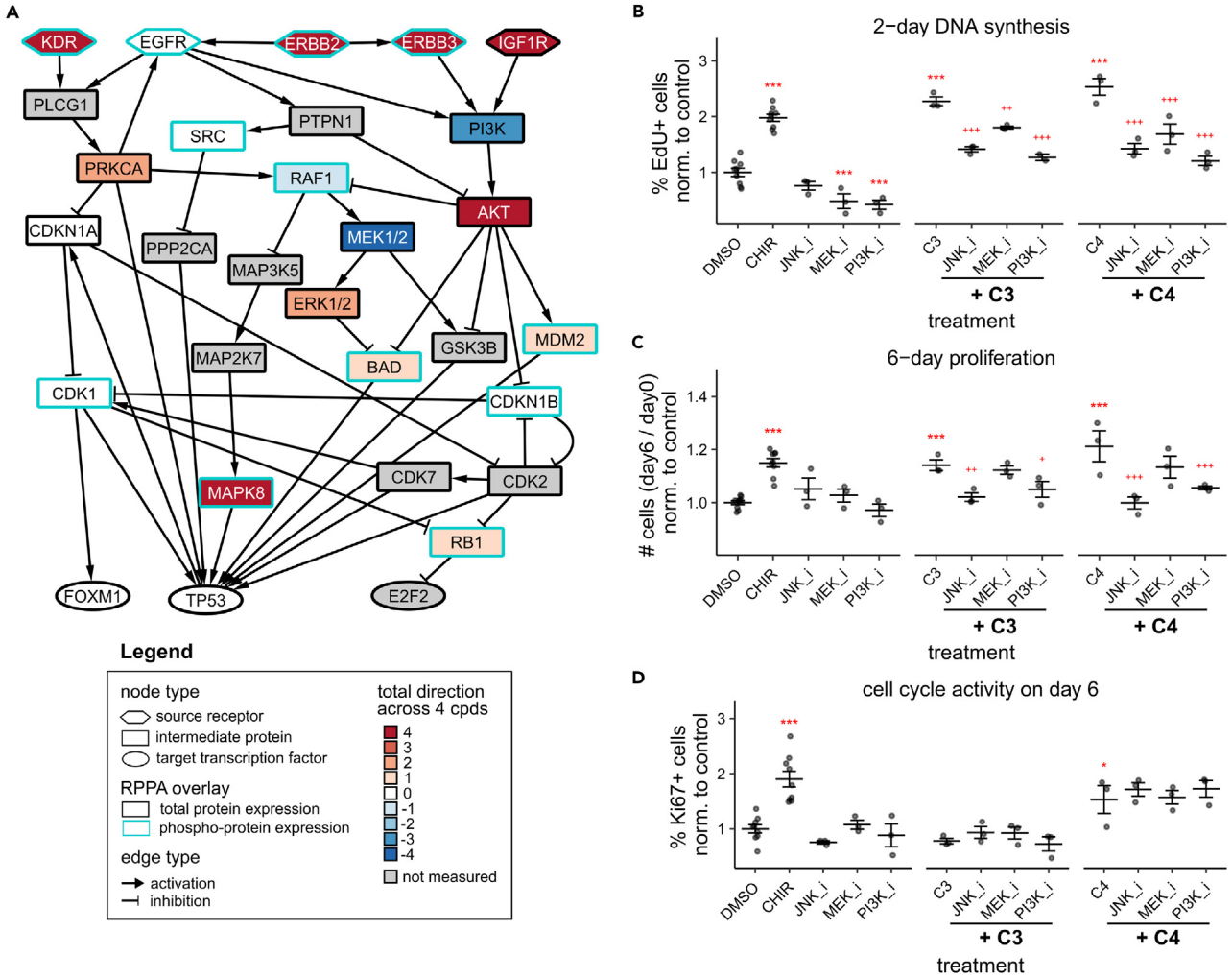

Figure 6. Network integrating transcriptomic and proteomic data identifies JNK and PI3K pathways mediate compound-induced proliferation of hiPSC-CMs

(A) Directed molecular network integrating common factors identified in the proteomic and transcriptomic data. Node colors represent the sum of the qualitative significance (up = 1, down = −1, not significant = 0) across all 4 cpds based on data from the RPPA or RTK array. Gray nodes indicate nodes that were not measured in the RPPA or RTK arrays.

(B) 48 h EdU assay measuring DNA synthesis rates.

(C) 6-day live-cell proliferation assay tracking cell counts.

(D) Ki67 staining measuring cell cycle activity. Treatments for (B–D): neg control (0.1% DMSO), pos control (1 μM CHIR99021), and small molecule inhibitors targeting JNK (10 μM SP600125), MEK (10 μM PD98059), and PI3K (10 μM LY294002) alone and in combination with 3.2 μM C3 or C4. Error bars represent mean ± s.e.m. Stats for (D–G) were assessed by one-way ANOVA with Benjamini-Hochberg FDR correction for select comparisons (* = all single treatments were compared to DMSO control; + = all combination treatments were compared to the respective lead compound C3 or C4); n = 3–9; *$p < 0.05$; **$p < 0.01$; ***$p < 0.001$.

arrest/exit, apoptosis, or polyploidization.[38–40] Cell-cycle arrest in postnatal mammalian cardiomyocytes has been linked to DNA damage from oxidative stress[41] or telomere dysfunction.[42] Perturbing signaling pathways to stimulate proliferation in cardiomyocytes can have unanticipated consequences. For example, GSK3 deletion in adult mouse cardiomyocytes induced cell cycle re-entry and polyploidization followed by the activation of the DNA damage response pathway and mitotic catastrophe.[43] In contrast, the lead compounds in our study promoted proliferation without signs of toxicity or enhanced polyploidization, suggesting the compounds may be activating DNA repair mechanisms to enable canonical cell cycle progression. The precise role of DNA repair mechanisms in promoting cardiomyocyte proliferation remains to be determined.

Functional proteomic arrays also identified a common set of differentially expressed proteins and phosphoproteins in response to multiple lead compounds. We found the compounds collectively upregulated and activated multiple RTKs including ErbB2, IGF1R, and VEGFR2. In murine neuronal cells, the activation of CB1R has been shown to transactivate EGFR, IGF1R, and VEGFR1 via a ligand-independent

mechanism to mediate downstream ERK activation.[44–46] Conversely, we found the inhibition of CB1R with compound C4 activated RTKs. This discrepancy can be explained by cell type-dependent ligand-biased signaling at CB1R by different cannabinoid agonists.[47,48] For example, a study found N-arachidonoylethanolamine-activated arrestin-mediated receptor recycling, while THC induced CB1R degradation.[47] Additionally, another study showed WIN55212-2 acted as an agonist for all Gi subtypes, while R-methanandamide acts as an inverse agonist for GI 1 and GI 2 and an agonist for GI 3.[49] Thus, it is unclear which CB1R downstream mechanism is inhibited by our C4 compound, which was previously characterized as either an inverse agonist or an antagonist to CB1R.[50] Additional studies are needed to elucidate the precise mechanisms by which our compounds activate RTKs.

We further investigated the role of the activated RTKs in mediating compound-induced proliferation. Studies have demonstrated ErbB2 signaling necessary and sufficient to induce DNA synthesis and proliferation without endoreplication in postnatal mouse cardiomyocytes.[25,51] In partial agreement with these previous studies by others, we found the pharmacological inhibition of ErbB2/EGFR attenuated both C3 and C4 compound-induced DNA synthesis without affecting proliferation and polyploidization. This suggests that ErbB2/EGFR signaling is necessary for compounds to stimulate cell cycle reentry at G1/S transition, but not to promote later-stage cell division.

Previous studies investigating the role of VEGF signaling in cardiomyocyte proliferation have been inconclusive and contradictory.[31–33] For example, one group showed VEGF gene transfer in a pig MI model resulted in significant increases in cardiomyocyte mitotic index and the number of cardiomyocyte nuclei without cytokinesis.[31] However, another group found treatment with recombinant VEGF did not induce DNA synthesis or proliferation *in vitro* in neonatal rat cardiomyocytes.[33] In our study, we found that while the pharmacological inhibition of VEGF receptors did not affect compound-induced DNA synthesis, VEGF receptor signaling mediated the pro-proliferative effects exerted by the compounds in hiPSC-CMs. Additional analysis revealed inhibiting VEGF receptor signaling induced binucleation, intermediate DNA content, and polyploidy in both unstimulated and stimulated hiPSC-CMs, suggesting increased expression of VEGF receptors protects against polyploidization and aberrant mitosis. Further experiments are needed to discern whether the increased intermediate DNA content results from increased aneuploidy.

Our reconstructed directed molecular network focused on connecting common proteomic and transcriptomic signatures downstream of the activated RTKs. Analysis of the network suggested canonical RTK signaling mediators JNK, MEK/ERK, and PI3K/AKT were involved in regulating compound-induced proliferation. JNK,[52,53] MEK/ERK,[1,54,55] and PI3K/AKT[27,56–58] have each been implicated in mediating cell cycle reentry, linking multiple pathways to cardiomyocyte proliferation. However, other studies discovered agents that stimulate cardiomyocyte proliferation independent of PI3K/AKT and MEK/ERK.[12,37,59] Therefore, we tested selective inhibitors to determine the requirement for mechanistic roles of these kinases in mediating proliferation and endoreplication. We found that the pharmacological inhibition of all three kinases attenuated C3 and C4-induced DNA synthesis. However, only JNK and PI3K activities were necessary for the compounds to induce the bona-fide proliferation of hiPSC-CMs. Future work could test additional kinase inhibitors to rule out concerns about their limited specificity. While RTK signaling pathways are known to converge on MAPK and PI3K modules, none of the kinases we investigated were found to mediate the VEGF receptor regulation of cardiomyocyte endoreplication. Additional studies are needed to identify how the VEGF receptor signaling is linked to endoreplication and other mechanisms induced by the compounds. For example, all four compounds induced expression of TAZ (Figure 4D), a member of the Hippo complex that is a well-established hub of cardiomyocyte proliferation.[60] Given the relative immaturity of hiPSC-CMs, future studies will be needed to test these compounds and proliferative mechanisms in adult CMs.

In summary, we identified a core set of mechanisms by which multiple compounds regulate the cell cycle progression of hiPSC-CMs. Our study identified multiple putative targets that negatively regulate proliferation without endoreplication, including ALK5 and CB1R. We also discovered the lead compounds that collectively activated RTKs (ErbB2/EGFR and VEGF receptors) and activated downstream JNK and PI3K pathways to regulate DNA synthesis, endoreplication, and cell division in hiPSC-CMs.

Limitations of the study

This study focused on the proliferation of human iPSC-derived CMs. The efficacy of these small molecules may vary depending on species, developmental stage, and *in vivo* context.

STAR★METHODS

Detailed methods are provided in the online version of this paper and include the following:

- KEY RESOURCES TABLE
- RESOURCE AVAILABILITY
  - Lead contact
  - Materials availability
  - Data and code availability
- EXPERIMENTAL MODEL AND STUDY PARTICIPANTS DETAIL
  - Cell culture
- METHOD DETAILS
  - DNA synthesis assay
  - Live-cell proliferation assay
  - Immunostaining

- Automated image acquisition
- Automated image analysis
- RNA sequencing
- RNA-seq analysis
- Phospho-RTK array
- Reverse phase protein array
- Network integration
- Synthesis of compounds C2, C5, and C5b

- QUANTIFICATION AND STATISTICAL ANALYSIS
  - Statistical analysis for phenotypic experiments

SUPPLEMENTAL INFORMATION

Supplemental information can be found online at https://doi.org/10.1016/j.isci.2024.110485.

ACKNOWLEDGMENTS

This work was supported by AstraZeneca, a grant from the University of Virginia-AstraZeneca Strategic Cardiovascular Alliance, the University of Virginia Pinn Scholar Award, and the National Institutes of Health (T32-HL007284, S10 OD021723, HL160665, HL162925). We thank Ewa Kubicka for performing the RTK arrays and Emily Farber for performing the RNA sequencing.

AUTHOR CONTRIBUTIONS

LAW, QDW, and JJS conceived and designed the study. LAW, BW, and EK performed the experiments. LAW, KLW, BW, and ST performed data analysis. OE and KLG provided annotations for AstraZeneca compounds. IB contributed to data interpretation. KG and ATP were selected and KLG provided compounds C1–C5 and C1a–C5e. LAW, KLW, BW, ST, MJW, SB, DLB, QDW, and JJS contributed to experimental design, data interpretation, and article revision. LAW and JJS wrote the article.

DECLARATION OF INTERESTS

OE, IB, KB, ATP, KLG, and QDW are current or former employees of AstraZeneca. This study was funded by AstraZeneca and by a grant from the University of Virginia-AstraZeneca Strategic Cardiovascular Alliance to JJS at the University of Virginia. The remaining authors declare no competing financial interests.

Received: June 6, 2022
Revised: March 27, 2024
Accepted: July 8, 2024
Published: July 11, 2024

REFERENCES

1. Uosaki, H., Magadum, A., Seo, K., Fukushima, H., Takeuchi, A., Nakagawa, Y., Moyes, K.W., Narazaki, G., Kuwahara, K., Laflamme, M., et al. (2013). Identification of chemicals inducing cardiomyocyte proliferation in developmental stage-specific manner with pluripotent stem cells. Circ. Cardiovasc. Genet. *6*, 624–633. https://doi.org/10.1161/CIRCGENETICS.113.000330.
2. Eulalio, A., Mano, M., Dal Ferro, M., Zentilin, L., Sinagra, G., Zacchigna, S., and Giacca, M. (2012). Functional screening identifies miRNAs inducing cardiac regeneration. Nature *492*, 376–381. https://doi.org/10.1038/nature11739.
3. Diez-Cuñado, M., Wei, K., Bushway, P.J., Maurya, M.R., Perera, R., Subramaniam, S., Ruiz-Lozano, P., and Mercola, M. (2018). miRNAs that Induce Human Cardiomyocyte Proliferation Converge on the Hippo Pathway. Cell Rep. *23*, 2168–2174. https://doi.org/10.1016/j.celrep.2018.04.049.
4. Titmarsh, D.M., Glass, N.R., Mills, R.J., Hidalgo, A., Wolvetang, E.J., Porrello, E.R., Hudson, J.E., and Cooper-White, J.J. (2016). Induction of Human iPSC-Derived Cardiomyocyte Proliferation Revealed by Combinatorial Screening in High Density Microbioreactor Arrays. Sci. Rep. *6*, 24637. https://doi.org/10.1038/srep24637.
5. Mills, R.J., Parker, B.L., Quaife-Ryan, G.A., Voges, H.K., Needham, E.J., Bornot, A., Ding, M., Andersson, H., Polla, M., Elliott, D.A., et al. (2019). Drug Screening in Human PSC-Cardiac Organoids Identifies Pro-proliferative Compounds Acting via the Mevalonate Pathway. Cell Stem Cell *24*, 895–907.e6. https://doi.org/10.1016/j.stem.2019.03.009.
6. Patterson, M., Barske, L., Van Handel, B., Rau, C.D., Gan, P., Sharma, A., Parikh, S., Denholtz, M., Huang, Y., Yamaguchi, Y., et al. (2017). Frequency of mononuclear diploid cardiomyocytes underlies natural variation in heart regeneration. Nat. Genet. *49*, 1346–1353. https://doi.org/10.1038/ng.3929.
7. Bensley, J.G., De Matteo, R., Harding, R., and Black, M.J. (2016). Three-dimensional direct measurement of cardiomyocyte volume, nuclearity, and ploidy in thick histological sections. Sci. Rep. *6*, 23756. https://doi.org/10.1038/srep23756.
8. Bergmann, O., Zdunek, S., Felker, A., Salehpour, M., Alkass, K., Bernard, S., Sjostrom, S.L., Szewczykowska, M., Jackowska, T., dos Remedios, C., et al. (2015). Dynamics of Cell Generation and Turnover in the Human Heart. Cell *161*, 1566–1575. https://doi.org/10.1016/j.cell.2015.05.026.
9. Windmueller, R., Leach, J.P., Babu, A., Zhou, S., Morley, M.P., Wakabayashi, A., Petrenko, N.B., Viatour, P., and Morrisey, E.E. (2020). Direct Comparison of Mononucleated and Binucleated Cardiomyocytes Reveals Molecular Mechanisms Underlying Distinct Proliferative Competencies. Cell Rep. *30*, 3105–3116.e4. https://doi.org/10.1016/j.celrep.2020.02.034.
10. González-Rosa, J.M., Sharpe, M., Field, D., Soonpaa, M.H., Field, L.J., Burns, C.E., and Burns, C.G. (2018). Myocardial polyploidization creates a barrier to heart regeneration in zebrafish. Dev. Cell *44*, 433–446.e7. https://doi.org/10.1016/j.devcel.2018.01.021.
11. Woo, L.A., Tkachenko, S., Ding, M., Plowright, A.T., Engkvist, O., Andersson, H., Drowley, L., Barrett, I., Firth, M., Akerblad, P.,

et al. (2019). High-content phenotypic assay for proliferation of human iPSC-derived cardiomyocytes identifies L-type calcium channels as targets. J. Mol. Cell. Cardiol. *127*, 204–214. https://doi.org/10.1016/j.yjmcc.2018.12.015.
12. Magadum, A., Ding, Y., He, L., Kim, T., Vasudevarao, M.D., Long, Q., Yang, K., Wickramasinghe, N., Renikunta, H.V., Dubois, N., et al. (2017). Live cell screening platform identifies PPARδ as a regulator of cardiomyocyte proliferation and cardiac repair. Cell Res. *27*, 1002–1019. https://doi.org/10.1038/cr.2017.84.
13. Sharma, A., Burridge, P.W., McKeithan, W.L., Serrano, R., Shukla, P., Sayed, N., Churko, J.M., Kitani, T., Wu, H., Holmström, A., et al. (2017). High-throughput screening of tyrosine kinase inhibitor cardiotoxicity with human induced pluripotent stem cells. Sci. Transl. Med. *9*, eaaf2584. https://doi.org/10.1126/scitranslmed.aaf2584.
14. Berenbaum, M.C. (1989). What is synergy? Pharmacol. Rev. *41*, 93–141.
15. Foucquier, J., and Guedj, M. (2015). Analysis of drug combinations: current methodological landscape. Pharmacol. Res. Perspect. *3*, e00149. https://doi.org/10.1002/prp2.149.
16. Chen, E.Y., Tan, C.M., Kou, Y., Duan, Q., Wang, Z., Meirelles, G.V., Clark, N.R., and Ma'ayan, A. (2013). Enrichr: interactive and collaborative HTML5 gene list enrichment analysis tool. BMC Bioinf. *14*, 128. https://doi.org/10.1186/1471-2105-14-128.
17. Kuleshov, M.V., Jones, M.R., Rouillard, A.D., Fernandez, N.F., Duan, Q., Wang, Z., Koplev, S., Jenkins, S.L., Jagodnik, K.M., Lachmann, A., et al. (2016). Enrichr: a comprehensive gene set enrichment analysis web server 2016 update. Nucleic Acids Res. *44*, W90–W97. https://doi.org/10.1093/nar/gkw377.
18. Keenan, A.B., Torre, D., Lachmann, A., Leong, A.K., Wojciechowicz, M.L., Utti, V., Jagodnik, K.M., Kropiwnicki, E., Wang, Z., and Ma'ayan, A. (2019). ChEA3: transcription factor enrichment analysis by orthogonal omics integration. Nucleic Acids Res. *47*, W212–W224. https://doi.org/10.1093/nar/gkz446.
19. Henning, E., Nadine, H., Petra, N., Herbert, N., Praveen, G., Andreas, S., Ursula, M.-W., Karl, W., and Braun, T. (2005). Divergent Siblings. Circ. Res. *96*, 509–517. https://doi.org/10.1161/01.RES.0000159705.17322.57.
20. Ebelt, H., Zhang, Y., Kampke, A., Xu, J., Schlitt, A., Buerke, M., Müller-Werdan, U., Werdan, K., and Braun, T. (2008). E2F2 expression induces proliferation of terminally differentiated cardiomyocytes in vivo. Cardiovasc. Res. *80*, 219–226. https://doi.org/10.1093/cvr/cvn194.
21. Sengupta, A., Kalinichenko, V.V., and Yutzey, K.E. (2013). FoxO1 and FoxM1 transcription factors have antagonistic functions in neonatal cardiomyocyte cell-cycle withdrawal and IGF1 gene regulation. Circ. Res. *112*, 267–277. https://doi.org/10.1161/CIRCRESAHA.112.277442.
22. Bolte, C., Zhang, Y., Wang, I.-C., Kalin, T.V., Molkentin, J.D., and Kalinichenko, V.V. (2011). Expression of Foxm1 transcription factor in cardiomyocytes is required for myocardial development. PLoS One *6*, e22217. https://doi.org/10.1371/journal.pone.0022217.
23. Korver, W., Schilham, M.W., Moerer, P., van den Hoff, M.J., Dam, K., Lamers, W.H., Medema, R.H., and Clevers, H. (1998). Uncoupling of S phase and mitosis in cardiomyocytes and hepatocytes lacking the winged-helix transcription factor Trident. Curr. Biol. *8*, 1327–1330. https://doi.org/10.1016/s0960-9822(07)00563-5.
24. Gründl, M., Walz, S., Hauf, L., Schwab, M., Werner, K.M., Spahr, S., Schulte, C., Maric, H.M., Ade, C.P., and Gaubatz, S. (2020). Interaction of YAP with the Myb-MuvB (MMB) complex defines a transcriptional program to promote the proliferation of cardiomyocytes. PLoS Genet. *16*, e1008818. https://doi.org/10.1371/journal.pgen.1008818.
25. D'Uva, G., Aharonov, A., Lauriola, M., Kain, D., Yahalom-Ronen, Y., Carvalho, S., Weisinger, K., Bassat, E., Rajchman, D., Yifa, O., et al. (2015). ERBB2 triggers mammalian heart regeneration by promoting cardiomyocyte dedifferentiation and proliferation. Nat. Cell Biol. *17*, 627–638. https://doi.org/10.1038/ncb3149.
26. Honkoop, H., de Bakker, D.E., Aharonov, A., Kruse, F., Shakked, A., Nguyen, P.D., de Heus, C., Garric, L., Muraro, M.J., Shoffner, A., et al. (2019). Single-cell analysis uncovers that metabolic reprogramming by ErbB2 signaling is essential for cardiomyocyte proliferation in the regenerating heart. Elife *8*, e50163. https://doi.org/10.7554/eLife.50163.
27. Bersell, K., Arab, S., Haring, B., and Kühn, B. (2009). Neuregulin1/ErbB4 Signaling Induces Cardiomyocyte Proliferation and Repair of Heart Injury. Cell *138*, 257–270. https://doi.org/10.1016/j.cell.2009.04.060.
28. Huang, Y., Harrison, M.R., Osorio, A., Kim, J., Baugh, A., Duan, C., Sucov, H.M., and Lien, C.-L. (2013). Igf Signaling is Required for Cardiomyocyte Proliferation during Zebrafish Heart Development and Regeneration. PLoS One *8*, e67266. https://doi.org/10.1371/journal.pone.0067266.
29. McDevitt, T.C., Laflamme, M.A., and Murry, C.E. (2005). Proliferation of cardiomyocytes derived from human embryonic stem cells is mediated via the IGF/PI 3-kinase/Akt signaling pathway. J. Mol. Cell. Cardiol. *39*, 865–873. https://doi.org/10.1016/j.yjmcc.2005.09.007.
30. Jennbacken, K., Wågberg, F., Karlsson, U., Eriksson, J., Magnusson, L., Chimienti, M., Ricchiuto, P., Bernström, J., Ding, M., Ross-Thriepland, D., et al. (2019). Phenotypic Screen with the Human Secretome Identifies FGF16 as Inducing Proliferation of iPSC-Derived Cardiac Progenitor Cells. Int. J. Mol. Sci. *20*, 6037. https://doi.org/10.3390/ijms20236037.
31. Laguens, R., Meckert, P.C., Janavel, G.V., Valle, H. del, Lascano, E., Negroni, J., Werba, P., Cuniberti, L., Martínez, V., Melo, C., et al. (2002). Entrance in mitosis of adult cardiomyocytes in ischemic pig hearts after plasmid-mediated rhVEGF 165 gene transfer. Gene Ther. *9*, 1676–1681. https://doi.org/10.1038/sj.gt.3301844.
32. Xu, X.H., Xu, J., Xue, L., Cao, H.L., Liu, X., and Chen, Y.J. (2011). VEGF attenuates development from cardiac hypertrophy to heart failure after aortic stenosis through mitochondrial mediated apoptosis and cardiomyocyte proliferation. J. Cardiothorac. Surg. *6*, 54. https://doi.org/10.1186/1749-8090-6-54.
33. Zentilin, L., Puligadda, U., Lionetti, V., Zacchigna, S., Collesi, C., Pattarini, L., Ruozi, G., Camporesi, S., Sinagra, G., Pepe, M., et al. (2010). Cardiomyocyte VEGFR-1 activation by VEGF-B induces compensatory hypertrophy and preserves cardiac function after myocardial infarction. Faseb. J. *24*, 1467–1478. https://doi.org/10.1096/fj.09-143180.
34. Perfetto, L., Briganti, L., Calderone, A., Cerquone Perpetuini, A., Iannuccelli, M., Langone, F., Licata, L., Marinkovic, M., Mattioni, A., Pavlidou, T., et al. (2016). SIGNOR: a database of causal relationships between biological entities. Nucleic Acids Res. *44*, D548–D554. https://doi.org/10.1093/nar/gkv1048.
35. Licata, L., Lo Surdo, P., Iannuccelli, M., Palma, A., Micarelli, E., Perfetto, L., Peluso, D., Calderone, A., Castagnoli, L., and Cesareni, G. (2020). SIGNOR 2.0, the SIGnaling Network Open Resource 2.0: 2019 update. Nucleic Acids Res. *48*, D504–D510. https://doi.org/10.1093/nar/gkz949.
36. Ritz, A., Poirel, C.L., Tegge, A.N., Sharp, N., Simmons, K., Powell, A., Kale, S.D., and Murali, T. (2016). Pathways on demand: automated reconstruction of human signaling networks. NPJ Syst. Biol. Appl. *2*, 16002. https://doi.org/10.1038/npjsba.2016.2.
37. Kühn, B., del Monte, F., Hajjar, R.J., Chang, Y.-S., Lebeche, D., Arab, S., and Keating, M.T. (2007). Periostin induces proliferation of differentiated cardiomyocytes and promotes cardiac repair. Nat. Med. *13*, 962–969. https://doi.org/10.1038/nm1619.
38. Jackson, S.P., and Bartek, J. (2009). The DNA-damage response in human biology and disease. Nature *461*, 1071–1078. https://doi.org/10.1038/nature08467.
39. Ivanov, A., Cragg, M.S., Erenpreisa, J., Emzinsh, D., Lukman, H., and Illidge, T.M. (2003). Endopolyploid cells produced after severe genotoxic damage have the potential to repair DNA double strand breaks. J. Cell Sci. *116*, 4095–4106. https://doi.org/10.1242/jcs.00740.
40. Baus, F., Gire, V., Fisher, D., Piette, J., and Dulić, V. (2003). Permanent cell cycle exit in G2 phase after DNA damage in normal human fibroblasts. EMBO J. *22*, 3992–4002. https://doi.org/10.1093/emboj/cdg387.
41. Puente, B.N., Kimura, W., Muralidhar, S.A., Moon, J., Amatruda, J.F., Phelps, K.L., Grinsfelder, D., Rothermel, B.A., Chen, R., Garcia, J.A., et al. (2014). The oxygen-rich postnatal environment induces cardiomyocyte cell-cycle arrest through DNA damage response. Cell *157*, 565–579. https://doi.org/10.1016/j.cell.2014.03.032.
42. Aix, E., Gutiérrez-Gutiérrez, Ó., Sánchez-Ferrer, C., Aguado, T., and Flores, I. (2016). Postnatal telomere dysfunction induces cardiomyocyte cell-cycle arrest through p21 activation. J. Cell Biol. *213*, 571–583. https://doi.org/10.1083/jcb.201510091.
43. Zhou, J., Ahmad, F., Parikh, S., Hoffman, N.E., Rajan, S., Verma, V.K., Song, J., Yuan, A., Shanmughapriya, S., Guo, Y., et al. (2016). Loss of Adult Cardiac Myocyte GSK-3 Leads to Mitotic Catastrophe Resulting in Fatal Dilated Cardiomyopathy. Circ. Res. *118*, 1208–1222. https://doi.org/10.1161/CIRCRESAHA.116.308544.
44. Dalton, G.D., Peterson, L.J., and Howlett, A.C. (2013). CB_1 cannabinoid receptors promote maximal FAK catalytic activity by stimulating cooperative signaling between receptor tyrosine kinases and integrins in neuronal cells. Cell. Signal. *25*, 1665–1677. https://doi.org/10.1016/j.cellsig.2013.03.020.
45. Dalton, G.D., and Howlett, A.C. (2012). Cannabinoid CB1 receptors transactivate multiple receptor tyrosine kinases and regulate serine/threonine kinases to activate ERK in neuronal cells. Br. J. Pharmacol. *165*,

2497–2511. https://doi.org/10.1111/j.1476-5381.2011.01455.x.
46. Rubovitch, V., Gafni, M., and Sarne, Y. (2004). The involvement of VEGF receptors and MAPK in the cannabinoid potentiation of Ca2+ flux into N18TG2 neuroblastoma cells. Brain Res. Mol. Brain Res. *120*, 138–144. https://doi.org/10.1016/j.molbrainres.2003.10.012.
47. Laprairie, R.B., Bagher, A.M., Kelly, M.E.M., Dupré, D.J., and Denovan-Wright, E.M. (2014). Type 1 cannabinoid receptor ligands display functional selectivity in a cell culture model of striatal medium spiny projection neurons. J. Biol. Chem. *289*, 24845–24862. https://doi.org/10.1074/jbc.M114.557025.
48. Khajehali, E., Malone, D.T., Glass, M., Sexton, P.M., Christopoulos, A., and Leach, K. (2015). Biased Agonism and Biased Allosteric Modulation at the CB1 Cannabinoid Receptor. Mol. Pharmacol. *88*, 368–379. https://doi.org/10.1124/mol.115.099192.
49. Mukhopadhyay, S., and Howlett, A.C. (2005). Chemically distinct ligands promote differential CB1 cannabinoid receptor-Gi protein interactions. Mol. Pharmacol. *67*, 2016–2024. https://doi.org/10.1124/mol.104.003558.
50. Plowright, A.T., Nilsson, K., Antonsson, M., Amin, K., Broddefalk, J., Jensen, J., Lehmann, A., Jin, S., St-Onge, S., Tomaszewski, M.J., et al. (2013). Discovery of agonists of cannabinoid receptor 1 with restricted central nervous system penetration aimed for treatment of gastroesophageal reflux disease. J. Med. Chem. *56*, 220–240. https://doi.org/10.1021/jm301511h.
51. Ma, H., Yin, C., Zhang, Y., Qian, L., and Liu, J. (2016). ErbB2 is required for cardiomyocyte proliferation in murine neonatal hearts. Gene *592*, 325–330. https://doi.org/10.1016/j.gene.2016.07.006.
52. Peng, X., Fan, S., Tan, J., Zeng, Z., Su, M., Zhang, Y., Yang, M., Xia, L., Fan, X., Cai, W., and Tang, W.H. (2020). Wnt2bb Induces Cardiomyocyte Proliferation in Zebrafish Hearts via the jnk1/c-jun/creb1 Pathway. Front. Cell Dev. Biol. *8*, 323. https://doi.org/10.3389/fcell.2020.00323.
53. Hammoud, L., Burger, D.E., Lu, X., and Feng, Q. (2009). Tissue inhibitor of metalloproteinase-3 inhibits neonatal mouse cardiomyocyte proliferation via EGFR/JNK/SP-1 signaling. Am. J. Physiol. Cell Physiol. *296*, C735–C745. https://doi.org/10.1152/ajpcell.00246.2008.
54. Bassat, E., Mutlak, Y.E., Genzelinakh, A., Shadrin, I.Y., Baruch Umansky, K., Yifa, O., Kain, D., Rajchman, D., Leach, J., Riabov Bassat, D., et al. (2017). The extracellular matrix protein agrin promotes heart regeneration in mice. Nature *547*, 179–184. https://doi.org/10.1038/nature22978.
55. Novoyatleva, T., Diehl, F., van Amerongen, M.J., Patra, C., Ferrazzi, F., Bellazzi, R., and Engel, F.B. (2010). TWEAK is a positive regulator of cardiomyocyte proliferation. Cardiovasc. Res. *85*, 681–690. https://doi.org/10.1093/cvr/cvp360.
56. Engel, F.B., Schebesta, M., Duong, M.T., Lu, G., Ren, S., Madwed, J.B., Jiang, H., Wang, Y., and Keating, M.T. (2005). p38 MAP kinase inhibition enables proliferation of adult mammalian cardiomyocytes. Genes Dev. *19*, 1175–1187. https://doi.org/10.1101/gad.1306705.
57. Lin, Z., Zhou, P., von, G.A., Gu, F., Ma, Q., Chen, J., Guo, H., van Gorp, P.R.R., Wang, D.-Z., and Pu, W.T. (2015). Pi3kcb Links Hippo-YAP and PI3K-AKT Signaling Pathways to Promote Cardiomyocyte Proliferation and Survival. Circ. Res. *116*, 35–45. https://doi.org/10.1161/CIRCRESAHA.115.304457.
58. Beigi, F., Schmeckpeper, J., Pow-anpongkul, P., Payne, J.A., Zhang, L., Zhang, Z., Huang, J., Mirotsou, M., and Dzau, V.J. (2013). C3orf58, a Novel Paracrine Protein, Stimulates Cardiomyocyte Cell Cycle Progression Through the PI3K-AKT-CDK7 Pathway. Circ. Res. *113*, 372–380. https://doi.org/10.1161/CIRCRESAHA.113.301075.
59. Yue, Z., Chen, J., Lian, H., Pei, J., Li, Y., Chen, X., Song, S., Xia, J., Zhou, B., Feng, J., et al. (2019). PDGFR-β Signaling Regulates Cardiomyocyte Proliferation and Myocardial Regeneration. Cell Rep. *28*, 966–978.e4. https://doi.org/10.1016/j.celrep.2019.06.065.
60. Heallen, T., Zhang, M., Wang, J., Bonilla-Claudio, M., Klysik, E., Johnson, R., and Martin, J. (2011). Hippo pathway inhibits Wnt signaling to restrain cardiomyocyte proliferation and heart size. Science (New York, N.Y.) *332*, 458–461. https://doi.org/10.1126/science.1199010.
61. Langmead, B., Wilks, C., Antonescu, V., and Charles, R. (2019). Scaling read aligners to hundreds of threads on general-purpose processors. Bioinformatics *35*, 421–432. https://doi.org/10.1093/bioinformatics/bty648.
62. Liao, Y., Smyth, G.K., and Shi, W. (2014). featureCounts: an efficient general purpose program for assigning sequence reads to genomic features. Bioinformatics *30*, 923–930. https://doi.org/10.1093/bioinformatics/btt656.
63. Love, M.I., Huber, W., and Anders, S. (2014). Moderated estimation of fold change and dispersion for RNA-seq data with DESeq2. Genome Biol. *15*, 550. https://doi.org/10.1186/s13059-014-0550-8.
64. Ritchie, M.E., Phipson, B., Wu, D., Hu, Y., Law, C.W., Shi, W., and Smyth, G.K. (2015). limma powers differential expression analyses for RNA-sequencing and microarray studies. Nucleic Acids Res. *43*, e47. https://doi.org/10.1093/nar/gkv007.
65. Gu, Z., Eils, R., and Schlesner, M. (2016). Complex heatmaps reveal patterns and correlations in multidimensional genomic data. Bioinformatics *32*, 2847–2849. https://doi.org/10.1093/bioinformatics/btw313.
66. Hothorn, T., Bretz, F., and Westfall, P. (2008). Simultaneous inference in general parametric models. Biom. J. *50*, 346–363. https://doi.org/10.1002/bimj.200810425.
67. Bass, G.T., Ryall, K.A., Katikapalli, A., Taylor, B.E., Dang, S.T., Acton, S.T., and Saucerman, J.J. (2012). Automated image analysis identifies signaling pathways regulating distinct signatures of cardiac myocyte hypertrophy. J. Mol. Cell. Cardiol. *52*, 923–930. https://doi.org/10.1016/j.yjmcc.2011.11.009.
68. Rosin, P.L. (2001). Unimodal thresholding. Pattern Recogn. *34*, 2083–2096. https://doi.org/10.1016/S0031-3203(00)00136-9.
69. Watson, J.V., Chambers, S.H., and Smith, P.J. (1987). A pragmatic approach to the analysis of DNA histograms with a definable G1 peak. Cytometry *8*, 1–8. https://doi.org/10.1002/cyto.990080101.
70. Dean, P.N., and Jett, J.H. (1974). Mathematical analysis of DNA distributions derived from flow microfluorometry. J. Cell Biol. *60*, 523–527. https://doi.org/10.1083/jcb.60.2.523.
71. Langmead, B., and Salzberg, S.L. (2012). Fast gapped-read alignment with Bowtie 2. Nat. Methods *9*, 357–359. https://doi.org/10.1038/nmeth.1923.
72. Smyth, G.K. (2004). Linear models and empirical bayes methods for assessing differential expression in microarray experiments. Stat. Appl. Genet. Mol. Biol. *3*, Article3. https://doi.org/10.2202/1544-6115.1027.
73. Ritchie, M.E., Phipson, B., Wu, D., Hu, Y., Law, C.W., Shi, W., and Smyth, G.K. (2015). limma powers differential expression analyses for RNA-sequencing and microarray studies. Nucleic Acids Res. *43*, e47. https://doi.org/10.1093/nar/gkv007.

CellPress
OPEN ACCESS

STAR★METHODS

KEY RESOURCES TABLE

REAGENT or RESOURCE	SOURCE	IDENTIFIER
Antibodies		
Rabbit polyclonal anti-Cardiac Troponin T	Abcam	cat# ab45932; RRID AB_956386
Rat monoclonal anti-Ki67	Invitrogen	cat# 14-5698-82; RRID AB_10854564
Chemicals		
Compounds C1-C5	AstraZeneca	see Table S1
Compounds C1a-C5e (functional analogs)	AstraZeneca	see Table S1
DAPI	Sigma	cat# D9542-5MG
Hoechst 33342	Invitrogen	cat# H3570
EdU	Invitrogen	cat# A10044
CHIR99021	Sigma-Aldrich	cat# SML1046
PD98059	TOCRIS	cat# 1213
Lapatinib	TOCRIS	cat #6811
LY294002	Selleckchem	cat# S1105
SP600125	Selleckchem	cat# S1460
Axitinib	Selleckchem	cat# S1005
Linsitinib (OSI-906)	Selleckchem	cat# S1091
AF 546 Azide (for EdU click chemistry)	Click Chemistry Tools	cat# 1283-1
William's E media, no phenol red	Gibco	cat# A1217601
Primary Hepatocyte Cell Maintenance Cocktail B	Gibco	cat# CM4000
iCell Cardiomyocytes Plating Medium	Cellular Dynamics International	cat# CMM-100-110-005
iCell Cardiomyocytes Maintenance Medium	Cellular Dynamics International	cat# CMM-100-120-005
Penicillin/Streptomycin	Gibco	cat# 15140122
Protease inhibitor cocktail	Sigma	cat# P8340
Commercial assays		
mirVana microRNA Isolation Kit, with phenol	Invitrogen	cat# AM1560
Proteome Profiler Human Phospho-RTK Array Kit	R&D Systems	cat# ARY001B
Deposited data		
Raw and analyzed RNA-seq data	This paper	GEO: GSE268693
Raw RPPA data	This paper	https://doi.org/10.6084/m9.figshare.26046337
Experimental models: Cell lines		
iCell Human iPSC-derived cardiomyocytes	Cellular Dynamics International	cat# CMC-100-010-001
Software and algorithms		
MetaMorph	Olympus	
Harmony	Perkin-Elmer	
MATLAB R2017B	Mathworks	
R v3.6.1	R Project	RRID:SCR_001905
Fast QC		RRID:SCR_014583
Bowtie2	Langmead et al.[61]	http://bowtie-bio.sourceforge.net/bowtie2/index.shtml

(*Continued on next page*)

Continued

REAGENT or RESOURCE	SOURCE	IDENTIFIER
featureCounts	Liao et al.,[62]	RRID:SCR_012919
DESeq2 v1.24.0	Love et al.[63]	RRID:SCR_015687
LIMMA v3.40.2	Ritchie et al.[64]	https://bioconductor.org/packages/release/bioc/html/limma.html
EnrichR	Chen et al.[16]	https://maayanlab.cloud/Enrichr/
ChEA3	Keenan et al.[18]	https://amp.pharm.mssm.edu/chea3/
ggplot2 v3.2.1		RRID:SCR_014601
ComplexHeatmap v2.0.0	Gu et al.[65]	http://bioconductor.org/packages/release/bioc/html/ComplexHeatmap.html
multcomp v1.4-13	Hothorn et al.[66]	http://multcomp.R-forge.R-project.org

RESOURCE AVAILABILITY

Lead contact

Further information and requests for resources and reagents should be directed to and will be fulfilled by the lead contact, Jeffrey J. Saucerman (jsaucerman@virginia.edu).

Materials availability

- The compounds corresponding to treatments named in the manuscript (C3/RepSox, CHIR99021 (aka CHIR), PD98059, LY294002, SP600125, lapatinib, axitinib, linsitinib, C1b/PRI-724, C1d/AZD2858, C2c/AZ628, C3a/SB525334, C3c/galunisertib, C4a/taranabant, C4c/AZD4472, C4d/rimonabant, C5a/indometacin, C5c/celecoxib, and C5e/SC560) are commercially available compounds.
- There are restrictions to the availability of compounds C1, C2, C4, and C5 due to AstraZeneca's intellectual property rights

Data and code availability

- RNA-seq data have been deposited at GEO under accession GSE268693 and are publicly available as of the date of publication. Accession numbers are listed in the key resources table. The DOI are listed in the key resources table. Microscopy data reported in this paper will be shared by the lead contact upon request.
- Reverse phase protein array data have been deposited at fighshare at https://doi.org/10.6084/m9.figshare.26046337.
- The original code is available in this paper's supplemental information.
- Any additional information required to reanalyze the data reported in this paper is available from the lead contact upon request.

EXPERIMENTAL MODEL AND STUDY PARTICIPANTS DETAIL

Cell culture

ICell Cardiomyocytes (Cellular Dynamics International) were seeded in 96-well or 384-well Corning CellBind plates at approximately $2.5x10^4$ to $3.5x10^4$ cells/cm^2. Cells were cultured for 2 days in iCell Cardiomyocytes Plating Medium (Cellular Dynamics International) supplemented with 1% Penicillin/Streptomycin (P/S; Gibco) followed by an additional 4 days in iCell Cardiomyocytes Maintenance Medium (Cellular Dynamics International) supplemented with 1% P/S. For all experiments, cells were first serum starved for 4 h and then treated in William's E medium without phenol red (Gibco) supplemented with Primary Hepatocyte Cell Maintenance Cocktail B (Gibco) containing P/S, ITS+, GlutaMAX, and HEPES. Cells were cultured for all experiments in a humidified environment at 37°C with 5% CO_2.

METHOD DETAILS

DNA synthesis assay

EdU incorporation and labeling with copper catalyzed click chemistry was used to measure DNA synthesis. Cells were treated in the presence of 1 μM EdU (Invitrogen) for 48 h, and subsequently fixed and permeabilized prior to incubation with the EdU click chemistry reaction mix – 100mM Tris HCL pH 7.0 (Gentrox), 4 mM $CuSO_4$ (Sigma), 100 mM ascorbic acid (Sigma), and 5 μM Alexa Fluor 546 Azide (Click Chemistry Tools). After labeling EdU, cells were stained with anti-Cardiac Troponin T (Abcam) and DAPI (Sigma).

Live-cell proliferation assay

To track the change in the number of live cells over 6 days, the cells were stained with a non-toxic concentration (0.02 μg/mL) of Hoechst 33342 (Invitrogen) and imaged immediately after treatment.[11] Treatment medium was replaced on day 3 to replenish nutrients, and the cells were

stained with Hoechst 33342 and imaged again on day 6. Images of the same fields of view were acquired at both initial and final timepoints by aligning the multi-well plates using distinct tracking markers in the upper-left and bottom-right most wells. After acquiring live-cell images on day 6, cells were fixed and stained with anti-Cardiac Troponin T, anti-Ki67 (Invitrogen), and DAPI for subsequent binucleation, DNA content, cell-cycle phase, and nuclear ploidy analyses.

Immunostaining

Cells were fixed with 4% paraformaldehyde (Ted Pella) for 15 min, permeabilized with 0.2% Triton X-100 (MP Biomedicals) for 10 min at room temperature (RT), blocked with 5% bovine serum albumin (Sigma) for 1 h at RT, and incubated with primary antibodies (see key resources table) overnight at 4°C. Cells were then rinsed with 1x PBS (Gibco) three times, blocked again with 2% goat or donkey serum (Invitrogen) for 1 h at RT, and incubated with secondary antibodies for 1 h. After antibody staining, cells were rinsed with 1x PBS three times and incubated with DAPI for 10 min at RT.

Automated image acquisition

Stained cells were imaged using either the automated Olympus IX81 inverted microscope with motorized functions and a 10X UPlanSApo 0.4 NA objective or the Operetta CLS high-content imaging system (PerkinElmer) with a 10× 0.3NA objective. For imaging with the Olympus system, multi-well imaging pipelines were developed and executed using MetaMorph software (Olympus) to automate image acquisition and stitching of multi-channel 2x2 mosaics with 10% overlap. For the Operetta system, one field of view was acquired per well using the Harmony high-content imaging software (PerkinElmer).

Automated image analysis

Custom image analysis and processing pipelines were developed and implemented in MATLAB to quantify the number of nuclei/cells, percent EdU positive objects, percent Ki67 positive objects, multinucleation, DNA content, cell cycle phases, and ploidy. Code is freely available (https://github.com/saucermanlab/Woo_JMCC_PMID30597148).

Segmentation

Nuclei stained with either Hoechst 33342 or DAPI were segmented using a pipeline adapted from our previous works in high-content imaging[11,67] and functions from MATLAB's Image Processing Toolbox. Briefly, image data was smoothed with an adaptive low-pass Wiener filter and transformed to a binary mask using a global threshold based on the mode and variance of the intensity values. Clumps of nuclei were separated by applying the watershed algorithm to the distance transform map of the complement of the binary mask.

Classification

The binary segmented mask and background subtracted images were used to calculate the mean intensities of Hoechst 33342, DAPI, Cardiac-Troponin T, EdU, and Ki67 staining for each segmented object. Nuclei with Hoechst 33342 or DAPI mean intensity values greater than 5 standard deviations above the population mean were excluded from all counts. Marker positivity thresholds were determined using Rosin's unimodal thresholding algorithm[68] on the mean intensity values for each segmented object.

Pharmacology metrics

Based on concentration-dependent responses of changes in cell number, we quantified area under the curve (AUC) as the sum of the relative changes in cell number across the five concentrations of compound. As a measure of potency, we performed cubic B-spline interpolation and then calculated the minimum concentration needed to achieve 50% of the maximum effect.

Multinucleation analysis

Multinucleated cells were identified based on the distance between neighboring nuclei. This distance threshold was determined using Cardiac-Troponin T staining to visualize cell borders. A morphological closing operation with a circular structuring element was applied to the binary segmented mask to merge and classify nuclei in multinucleated cells.

Ploidy and cell cycle phase analysis

Our previous k-means clustering approach for measuring DNA content[11] was modified to identify nuclei with intermediate DNA content (3c) in addition to the 2c, 4c, and >4c nuclei. The updated algorithm was adapted from classical flow cytometry DNA content analysis approaches[69,70] using the histogram of integrated intensity measurements of DAPI or Hoechst 33342 segmented objects. Briefly, Gaussian distribution functions were fitted to the 2c and 4c peaks of DNA content, and the 3c population was estimated using a uniform distribution with height set to the average binned frequencies between the peaks. Ki67 staining was used to discriminate between actively cycling nuclei or nuclei in G0. Combining DNA content analysis and Ki67 positivity enabled classification of nuclei into 6 cell cycle phase and ploidy states – G1 (2c), S (3c), G2/M (4c), G0 (2c), G0 with intermediate DNA content (3c), and G0 tetraploid (4c).

RNA sequencing

Total RNA was isolated from hiPSC-CMs treated for 24 h using the mirVana microRNA Isolation Kit with phenol (Invitrogen) according to the manufacturer's guidelines. Each sample was run with 3 biological replicates. RNA integrity was assessed using the Agilent 2100 Bioanalyzer with the Agilent RNA 6000 Pico Kit by the University of Virginia's Genomics Core. All samples had RIN values ranging from 9.9 to 10.0. RNA sequencing libraries were generated and indexed using 200 ng of total RNA and the TruSeq Stranded mRNA LT Sample Prep Kit - Set B (Illumina) following the protocol provided by the manufacturer. Resulting libraries were then assessed using the Agilent TapeStation 4200 (Agilent Technologies) and quantified by Qubit 2.0 (Thermo Fisher Scientific). The indexed libraries were pooled at equal molar concentrations and paired-end sequenced with 75 bp per read on the Illumina NextSeq 500 system using NextSeq 500 High Output 150 cycle cartridges (Illumina).

RNA-seq analysis

Sequence read quality was assessed using the FastQC software (http://www.bioinformatics. babraham.ac.uk/projects/fastqc). All samples at all positions had Phred scores greater than 30. Paired-end reads were mapped to the human reference genome hg38 using the Bowtie2 aligner[71] and gene-level counts were quantified using the featureCounts program.[62] Genes with low counts were removed before normalizing by TMM. Normalized gene counts were voom transformed for principal component analysis. DESeq2[63] was used for differential gene expression analysis between compound-treatment and the negative control with an FDR significance level of 0.05. Pathway enrichment of differentially expressed gene sets was performed using EnrichR API platform with the Reactome 2016 database.[16,17] Transcription factor enrichment analysis was performed using ChEA3 API platform with the ARCHS4 co-expression database.[18]

Phospho-RTK array

Cells were seeded in 60 mm Corning CellBind dishes, cultured for 6 days, serum starved for 4 h, and treated with compounds for 12 h with 3 replicates. At the end of the experiment, cells were treated with 1mM peroxyvanadate (1 mM $NaVO_3$, 0.1 μg/mL Catalase, 0.003% H_2O_2) for 15 min prior to cell lysis. Cells were then rinsed with ice-cold 1x PBS and lysed on ice for 15 min with lysis buffer (50 mM Tris-HCl pH 7.5, 150 mM NaCl, 0.1 mM EDTA, 1mM DTT, 1mM NaVO3, 0.5% Triton X-100) containing protease inhibitor cocktail (Sigma). Cell lysates were mechanically homogenized using 28-gauge syringes, spun down, and adjusted to equivalent concentrations. The Proteome Profiler Human Phospho-RTK Array Kit (R&D Systems) was used to measure phosphorylation activity of 49 RTKs. Briefly, the arrays with printed anti-RTK antibodies were blocked for 1 h and incubated with 38.8 μg of total protein lysate overnight at 4°C. The arrays were then washed and incubated with anti-phospho-tyrosine antibodies conjugated to HRP and detected via chemiluminescence. Array films were scanned and Image Studio software (LI-COR) was used to quantify intensities of each spot. Intensity values were background subtracted and normalized to the positive control spots on each array.

Reverse phase protein array

The same cell lysates prepared for the RTK array were also used for the RPPA to measure protein and phospho-protein expression levels of over 250 proteins. The RPPA was performed and quantified by the University of Texas MD Anderson Cancer Center's Functional Proteomics RPPA Core. The MD Anderson platform included 240 total protein and 65 phospho-protein probes. Briefly, serial dilutions of lysates were printed on nitrocellulose-coated slides and each slide was probed with a different antibody. Signals were detected by tyramide signal amplification and DAB colorimetric reaction systems. Images of scanned slides were quantified by Array-Pro Analyzer. Relative protein levels were determined using the SuperCurve program (https://bioinformatics.mdanderson.org/public-software/supercurve/) and normalized to correct for protein loading and antibody variation. Linear models with the empirical Bayes[72] approach via the limma package[73] was used to assess differential expression in the RPPA between compounds and the DMSO negative control with an adjusted *p*-value significance level of 0.1.

Network integration

To reconstruct a directed network integrating the multi-omic signature, we used SIGNOR's manuallyannotated database of causal relationships linking biological factors.[34,35] We filtered the database to include relationships involving the set of common factors and their first neighbors, and excluded relationships with confidence scores less than 0.2. Next, we used the k shortest path algorithm from PATHLINKER,[36] with k = 20, to identify the pathways linking ErBB2, IGF1R, or VEGFR2 to the set of top 15 predicted transcription factors overlapping the set of proteins included in the filtered relationships. The shortest paths networks for each RTK were then merged and redundant relationships were removed. To visualize the overall proteomic responses on the network, each protein in the RPPA or RTK was assigned +1 for upregulated, −1 for downregulated, or 0 for not significant. We then mapped the sum of the signal direction onto the network nodes. For example, a node with value of +4 indicates the protein was upregulated across all four compounds.

Synthesis of compounds C2, C5, and C5b

All compounds had a purity of ≥95% as estimated from 1H NMR spectra and/or the HPLC UV trace. HRMS were recorded on a Micromass LCT MS equipped with an ESI. 1H NMR measurements were performed on Bruker Avance 300, 400 and 500 spectrometers, operating at 1H frequencies of 300, 400 and 500 MHz, respectively. The experiments were typically recorded at 25°C. Chemical shifts are given in ppm with the solvent as internal standard or TMS if added. Protons on heteroatoms such as NH and OH protons are only reported when detected in NMR

and may therefore be missing. Flash chromatography was performed using either normal phase silica FLASH+ (40M, 25M or 12M), Biotage SNAP Cartridges KP-Sil (340, 100, 50 or 10), or Agela Flash Column Silica-CS Cartridges (330, 180, 120, 80) unless otherwise stated. All solvents used were commercially available and of analytical grade. Anhydrous solvents were routinely used for reactions. The IUPAC names were generated using ChemDraw Professional version 19.0.0–22.2.0 from PerkinElmer. Details of synthesis are shown in Figure S7 (C2) and Figure S8 (C5 and C5b), with NMR spectra in Figures S9–S15.

QUANTIFICATION AND STATISTICAL ANALYSIS

Statistical analysis for phenotypic experiments

Phenotypic experiments were performed with 2–4 replicates for perturbation groups and 6–24 replicates for control groups. Measurements from experiments requiring multiple multi-well plates were normalized to the negative control wells in each plate. All statistical tests were implemented in R using the stats and multcomp v1.4-13 packages in R v3.6.1. Statistical significance was determined for experiments with multiple treatments using a one-way ANOVA with post-hoc test for multiple comparison correction (Dunnett, Benjamini-Hotchberg). Plots were generated in R using ggplot2 v3.2.1, ComplexHeatmap v2.0.0, cowplot v1.0.0, and VennDiagram v1.6.20. Error bars represent mean $\pm$ s.e.m. The number of replicates, statistical tests, and significance levels for phenotypic experiments are noted in the figure legends.